

Counting Statistics of a Bose-Einstein Condensate in a Double-Well Potential

by

Katrina Smith-Mannschott

Class of 2008

A thesis submitted to the  
faculty of Wesleyan University  
in partial fulfillment of the requirements for the  
Degree of Bachelor of Arts  
with Departmental Honors in Physics

# Abstract

This thesis aims to investigate the dynamic properties of ultra-cold Bose-Einstein condensates (BEC) trapped in a deep double well potential. Despite its simplicity, this system shows a rich variety of dynamical behaviors: Josephson oscillations, self-trapping behavior and critical dynamics. In contrast to previous studies, we aim to understand not only the first moment of the evolving occupation probability, but all its moments. This is known in mesoscopic physics as the "counting statistics" problem. Using the quantum dimer, we are the first to address the effects of interatomic interactions on counting statistics. We expect that our predictions will be easily tested in recent experimental realizations of the BEC double well trap.

# Acknowledgments

I would like to thank all of the people who made writing this thesis possible.

I am very grateful to all of the members of the Complex Quantum Dynamics and Mesoscopic Phenomena Group at Wesleyan University. Of these, Gim Seng Ng and Joshua Bodyfelt have been indispensable in getting me, the "newbie," up to speed with the physics and the supercomputer.

My housemates, Diana Shum, Melanie Cherng, and Maya Bery, have also all played a vital role in making this thesis possible. They have provided hugs, laughs, and comfort as needed throughout this process. Without their caring support, I would not have been able to finish this project.

I would also like to thank my family. My cousin Cynthia Volkert has always provided sound advice and a unique perspective about my future in physics. I thank my mother for her life-long support. Benjamin Smith-Mannschott, my brother, has supplied a vital programming and scripting help throughout this process. I would like to acknowledge my father as well, though his death prevented him from being a part of my career at Wesleyan University. Our shared humor has gotten me through many difficult days this year.

Thank you to the professors in the physics department. I have learned a great deal from each of them. Thanks to Fred Ellis, who gave me my first experiences with research at Wesleyan. Wesleyan University is gratefully acknowledged for financial support. Financial support from the USA Israel Binational Science Foundation (BSF) is also acknowledged.

I am deeply grateful to both Moritz Hiller and Tsampikos Kottos. Their help enabled to me to learn a vast amount since joining the CQDMP group at Wesleyan this past

summer. I also thank them for their great enthusiasm for physics. Additionally, they have both provided critical help in editing this work. Thank you so much.

Finally, I want to thank Alexander Foss. He has been wonderfully tolerant and supportive during this entire process. His loving support provided a much needed balance to all of this work.

# Contents

1	Introduction	7
2	Cold Bosons Interacting on a Lattice	10
2.1	Bose-Einstein Condensation	10
2.2	Optical Lattices	13
2.3	Bose-Hubbard Hamiltonian	15
2.4	The Classical Limit of the Bose-Hubbard Hamiltonian and the Discrete Non-linear Schrödinger Equation	17
2.5	The Bose-Hubbard Hamiltonian in Fock-space	19
2.6	Applications of the Bose-Hubbard Hamiltonian and the DNLS	20
3	Bose-Einstein Condensate trapped in a double-well potential: Stationary States	22
3.1	Bose-Hubbard Dimer	22
3.2	Classical Stationary States	23
3.3	Quantum Mechanical Perturbation Theory	25
3.3.1	Small coupling regime	25
3.3.2	Small interatomic interaction regime	30
4	Dynamics of the dimer	35
4.1	The Heidelberg Experiment	35
4.2	Wavepacket Dynamics: Classical Considerations	38
4.3	Wave Packet Dynamics: Quantum Calculations	42
4.3.1	The non-interacting limit	45
4.3.2	The small coupling regime	46

*Contents*

4.3.3	The small interatomic interaction regime . . . . .	52
4.4	Semiclassical Analysis . . . . .	56
5	Conclusions	63
A	Quantum Mechanical Conservation of the Total Number of Particles, $N$ , in the Dimer	64
B	Perturbation Theory in the Small Nonlinear Interaction Regime	66
C	The Time Evolution of $J_z$ to First Order in Small Interatomic Interaction Perturbation Theory	69

# 1 Introduction

Bose-Einstein condensation of ultra-cold atoms is a topic which currently is very popular, both in theoretical and experimental research. The most fascinating of these experimental accomplishments was the realization of Bose-Einstein condensation (BEC) of ultra-cold atoms in optical lattices [2, 6, 35] and the creation of “atom chips” [22] which have been suggested as potential building blocks for quantum information processing [38]; while at the same time allowing for novel, concrete applications of quantum mechanics, such as atom interferometers [39], transistors [32] and atom lasers [21]. In fact, the emerging field of atomtronics, i.e. the atom analogue of electronic materials, devices, and circuits, is predicted to be able to provide much more powerful devices than solid state ones. Atomtronics can be controlled to an extraordinary degree of precision, with respect not only to the confining potential, but also to the strength of the interaction between atoms, their preparation, and the measurement of the atomic cloud.

The aim of this thesis is to investigate the dynamics of small lattices, paying particular attention to the quantum fluctuations of the atomic populations. This problem is known as the counting statistics problem within the mesoscopic community. Although our long-term goal is to understand the counting statistics of large lattices, currently we will focus on the simplest possible construction, which is the dimer trap. The goal here is to identify how interatomic interactions affect the tunneling process. Our motivation for this study stems from a recent experiment by the Heidelberg group [1] in which they were able to measure and study the time evolution of the atomic population for a two well trap.

This thesis is structured as follows:

- *Chapter 2* will set up the mathematical and physical framework for the description of bosons on an optical lattice. It will begin with a brief introduction of the his-

## 1 Introduction

tory which lead to realization of Bose-Einstein condensation, including the basic concepts behind creating a BEC. Furthermore, it will discuss how the BEC can be manipulated using optical lattices. We then introduce the Bose-Hubbard Hamiltonian (BHH) which is the standard mathematical model that describes a BEC in a deep optical lattice. We go on to discuss the classical limit of the BHH, known as the Discrete Non-Linear Schrödinger (DNLS) equation. Finally, we give a brief overview of various physical applications of the BHH and the DNLS equation.

- *Chapter 3* focuses on the analysis of the stationary properties of the dimer. First we analyze the stationary states in the classical limit by solving the time-independent DNLS equation. We then compare to the numerical results obtained from the exact diagonalization of the BHH. Then we use quantum mechanical perturbation theory to try and analytically match the quantum numerics. We approach the perturbation theory from two limits: (a) the small coupling regime, which has been explored by Kalosakas, et al., in Ref. [25, 26, 27] and (b) the small interatomic interaction regime, which has, as of yet, not been investigated. Finally, we overplot the two perturbation theories on the exact numerical results to assess their validity.
- In *Chapter 4*, we move on to analyzing the dynamics of the BEC in a dimer trap. We begin by summarizing some of the recent experimental work by the Heidelberg group (see Ref. [1, 33]), and emphasizing its importance and relevance to our work. We then go on to do wavepacket analysis for the classical limit of the BHH, during which we explain the existence of 3 distinct dynamical regimes: Josephson oscillations, self-trapping, and critical dynamics (the transition point between the Josephson and self-trapping regimes). In order to analytically describe the quantum evolution of the atomic population, we explore the time-dependent perturbation theory for the small coupling regime and the small interatomic interaction regime. We end the chapter by incorporating a semiclassical calculation that captures the essential features of the quantum dynamics in all the regimes. Meticulous comparisons between the results of the quantum evolution and the semi-classical prediction indicate the strengths of the semiclassical method.

## *1 Introduction*

Although the first moment of the atom distribution has been exhaustively studied in past work, the merit of this thesis is that it aims to understand the whole distribution, i.e. all moments. We expect that our predictions will be confirmed experimentally in the very near future and we hope that they will shed some fresh light upon more complicated geometries, while providing new insights into the counting statistics of interacting particles.

## 2 Cold Bosons Interacting on a Lattice

This chapter is dedicated to presenting a mathematical and physical foundation for this thesis. We begin with a brief summary of the history leading up to the realization of Bose-Einstein condensation. Next, in §2.2, we give a short overview of how optical lattices can be used to manipulate Bose-Einstein condensates. In §2.3, we present the Bose-Hubbard Hamiltonian in second quantization. In §2.4, we then discuss the appropriate semiclassical limit of the BHH, thereby deriving the Discrete Non-Linear Schrödinger (DNLS) equation. Next, we show how to represent bosons trapped in a lattice potential using Fock-space in §2.5. Finally, in §2.6, we discuss a few important physical systems which are represented by Bose-Hubbard Hamiltonian and its classical limit, the DNLS equation.

### 2.1 Bose-Einstein Condensation

A series of ideas from various physicists led to the conceptualization and then realization of the Bose-Einstein condensate (BEC). In 1901, Max Planck published a paper in which he described his formula for the distribution of energy in black-body radiation [5]. Planck arrived at his law of black-body radiation primarily by guessing that energy quanta (i.e. photons) existed. However, though he used the concept of energy quanta, he did not fully understand its implications for physics. Planck attributed the need to use quantization to a mathematical artifact [29]. It was Albert Einstein who emphasized the importance of quantum theory by publishing a series of papers, most notably his theory of light quanta (or photons) in 1905.

After the publication of Planck's law of black-body radiation in 1901, many scientists,

including Einstein, tried to derive it from basic principles. However, all the attempted derivations were based in some way on classical mechanics [5]. Satyendra Nath Bose saw this as a logical fallacy, since the crux of Planck's proof rested on the use of energy quanta, which were foreign to classical mechanics. In 1924, Bose used Einstein's concept of photons to prove Planck's law of black body radiations [5]. He assumed that each quantum energy state could be occupied by any number of photons. Einstein then used this idea to predict the existence of a new type of phase transition, which came to be known as Bose-Einstein condensation [15, 16].

Einstein postulated that, like the photons described in Bose's paper, integer spin (bosonic) atoms do not obey the Pauli exclusion principle, thus allowing an arbitrary number of identical bosons to be piled into the same quantum state. Einstein further speculated that when a cloud of bosons was cooled below a critical temperature,  $T_c$ , the atoms would condense down to the lowest energy quantum state. During this cooling process, the de Broglie wavelength,  $\lambda_{dB} = (2\pi\hbar^2/k_B m T)^{1/2}$ , grows and thus the wave functions of the atoms smear and eventually overlap. This allows the wave function which describes the whole cloud of  $N$  bosons to reduce to a product of  $N$  identical single-particle ground state wave functions [47]. This process is illustrated in Fig. 2.1.

Though predicted in 1925, it was not until 1995 that Bose-Einstein condensation was realized. The first two groups to observe an "ideal" BEC were Wieman/Cornell [3] and Ketterle [13] (See Fig. 2.2). Although the concept behind creating a BEC seems trivial - that is, to make a cloud of bosons as cold as possible - in practice it proved to be quite difficult. There were two big obstacles which stood in the way of achieving a BEC. The first hinderance was that researchers had to ensure that as they lowered the temperature of the atom cloud, the gas did not transition to the more familiar phases: liquid and solid. This more conventional condensation can only be avoided at very low densities [28]. Thus researchers had to make certain that they were working with atoms which could be cooled to a BEC.

The second obstacle to realizing the BEC was figuring out how to trap and cool the atom cloud. Each time researchers got close to achieving a BEC, they ran into more technical difficulties. It was only in the 1980s that a breakthrough was made in laser

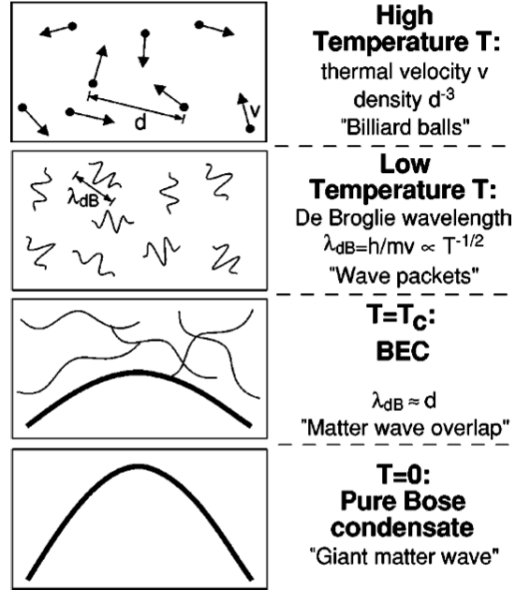


Figure 2.1: Criterion for Bose-Einstein condensation. At high temperatures, a weakly interacting gas can be treated as a system of "billiard balls." In a simplified quantum description, the atoms can be regarded as wave packets with an extension of their de Broglie wavelength  $\lambda_{dB}$ . At the BEC transition temperature,  $\lambda_{dB}$  becomes comparable to the distance between atoms, and a Bose condensate forms. As the temperature approaches zero, the thermal cloud disappears, leaving a pure Bose condensate. Figure taken from [28].

cooling techniques by W.D. Phillips, S. Chu, and C. Cohen-Tannoudji, all of whom were awarded the Nobel Prize [9]. The laser cooling technique is based on the use of the Doppler effect. Two counter propagating lasers, which are tuned to a frequency just below the resonance frequency of the atoms in the cloud, are set up to create a standing wave. The cloud of atoms is placed in this standing wave and at low intensities the atoms feel two opposite forces from the two lasers. The two opposing forces create a frictional force on atoms, slowing them down (i.e. cooling them) [10]. Via laser cooling, the atomic cloud can be cooled to the order of a few microkelvin [10]. However, a few microkelvin is still too 'hot' to create a BEC. Thus, a secondary cooling technique needed to be utilized.

In order to realize a BEC, the atom cloud is further cooled via a technique known as evaporative cooling. The pre-cooled atom cloud is then moved to a magnetic trap [33]. Next, the trap depth is reduced, allowing the more energetic (i.e. hotter) atoms to

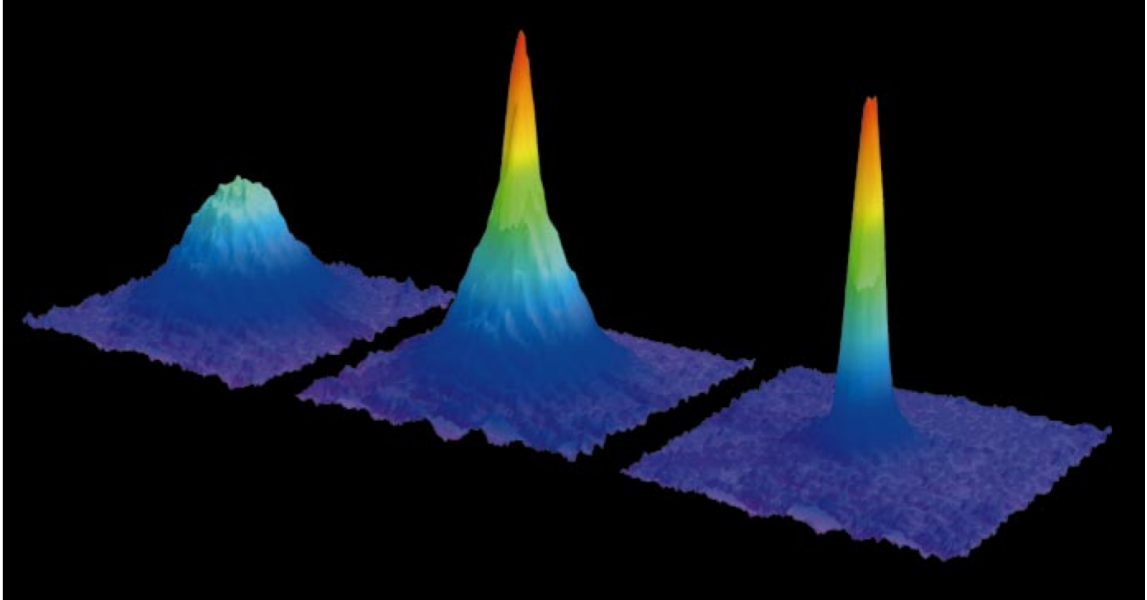


Figure 2.2: Observation of Bose-Einstein condensation by absorption imaging. Shown is absorption vs two spatial dimensions. The Bose-Einstein condensate is characterized by its slow expansion observed after 6 ms time of flight. The left picture shows an expanding cloud cooled to just about the transition point; middle: just after the condensate appeared; right: after further evaporative cooling has left an almost pure condensate. The total number of atoms at the phase transition is about  $7 \times 10^5$ , the temperature at the transition point is  $2 \mu\text{K}$ . Figure taken from [28].

escape, while the colder atoms stay behind. The remaining atoms rethermalize and then the trap depth is reduced again. This is repeated until the atom cloud reaches  $500\text{nK}$  to  $2 \mu\text{K}$ , at which point, the cloud collapses into a Bose-Einstein condensate [28].<sup>1</sup>

## 2.2 Optical Lattices

Since the BEC was achieved, many experimental developments have deepened our understanding of fundamental aspects of quantum physics, while simultaneously allowing us to investigate complicated theoretical scenarios with potential technological applications. The most fascinating of these experimental achievements was the realization of Bose-Einstein condensation (BEC) of ultra-cold atoms in optical lattices (OL), which have been suggested as potential building blocks for quantum information processing. At

<sup>1</sup>An applet which provides a visual understanding of evaporative cooling is available at: <http://www.colorado.edu/physics/2000/applets/bec.html>. Accessed: 2007-12-10.

## 2 Cold Bosons Interacting on a Lattice

the same time the precise tailoring and manipulation of OLs has allowed us to investigate complex solid state phenomena, such as the Mott-Insulator to superfluid transition, the Josephson effect, the atom blockade phenomenon in quantum-dot-like potentials, Anderson localization, and Bose-Glass transitions. In fact, it is anticipated that the emerging field of atomtronics will be able to provide much more powerful devices than the current solid-state ones, in which imperfections and decoherence quickly destroy the delicate quantum effects. (See Ref. [33] and references therein.)

During research into laser cooling techniques, it was found that the interfering lasers created an egg carton-like potential [33], which was then utilized to create what is known as an optical lattice. Optical lattices function on the basis of the AC Stark effect. The light field of the laser creates an oscillating electric field, which, in turn, induces an electrical dipole moment in each of the atoms in the BEC. An energy shift,  $\Delta E$ , is created by the interaction of electric dipole moments of the atoms and the laser's electric field,  $E(t)$ . The energy shift is [33]

$$\Delta E = -\frac{1}{2}\alpha(\omega)\langle E^2(t)\rangle \quad (2.1)$$

where  $\alpha$  is the polarizability of the atomic level which resonates at  $\omega_0$ . In  $\Delta E$ ,  $\omega = \omega_0 + \Delta$ , where  $\Delta$  is the detuning of the light field from the resonant frequency of the atoms. The induced dipole moment,  $D = \alpha(\omega)E$  [33], will be in phase with the electric field if the detuning is negative, i.e.  $\omega < \omega_0$ , thus making the potential minimized where the laser intensity is maximized. On the other hand, if the detuning is positive, i.e.  $\omega_0 < \omega$ , then the potential will be minimized where the laser intensity is minimized. The latter situation is easier to control in an experimental situation and thus it is preferable to have a positive detuning.

The detuning along with the peak intensity of the laser,  $I_P$ , provides control over the depth of the lattice sites,  $V_0$ , as [33]

$$V_0 \propto \frac{I_P}{\Delta} = \frac{I_P}{\omega - \omega_0} \quad (2.2)$$

Since we are working with a BEC, particle-particle collisions are estimated to have

an energy transfer so small that none of the particles get excited into a higher energy level, thus keeping the system in the ground state. When using an optical lattice to trap the BEC, spontaneous photon-particle scattering, i.e. the rate at which photons push particles into a higher energy state, also needs to be taken into account and avoided. The spontaneous scattering rate of atoms at the center of a trap is proportional to  $\frac{I_p}{\Delta^2}$  [33]. Thus, a large detuning will cause the spontaneous scattering to be negligible in comparison to the depth of the lattice sites.

The potential created by two interfering lasers with a wavelength  $\lambda_L$  is [33]

$$V(x) = V_0 \cos^2\left(\frac{2\pi x}{\lambda_L}\right)$$

where  $\lambda_L/2$  is the distance,  $d$ , between the two minima in the direction of the laser beam. This relationship is illustrated in Fig. 2.3. So, either by placing two counter propagating laser beams opposite to one another as shown in Fig. 2.3a or by adjusting a phase difference between the two lasers by changing  $\theta$  as in Fig. 2.3b, the depth of the wells can be adjusted. Therefore, we can adjust the potential depth in addition to the detuning, allowing us to minimize both the photon-particle and the particle-particle interactions which would excite the system out of the ground state.

## 2.3 Bose-Hubbard Hamiltonian

The simplest non-trivial model that describes interacting bosons on a lattice of  $s$  wells or sites, is the Bose-Hubbard Hamiltonian (BHH) which incorporates the competition between the kinetic and the interatomic interaction energy of the bosonic system. Due to the low density of the gas needed to achieve a BEC, the number of three-body collisions is negligible, allowing us to consider only two-body scattering events, which can be described sufficiently by  $s$ -wave scattering due to the low energies of the involved particles [12]:

$$\hat{H} = \sum_{i=1}^s \varepsilon_i \hat{n}_i + \frac{1}{2} \sum_{i=1}^s U_i \hat{n}_i (\hat{n}_i - 1) - \sum_{i,j} k_{i,j} [\hat{b}_i^\dagger \hat{b}_j + \hat{b}_j^\dagger \hat{b}_i], \quad (2.3)$$

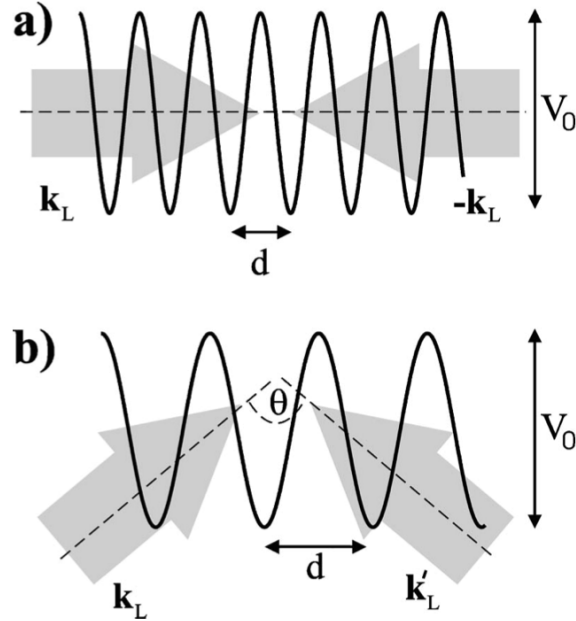


Figure 2.3: A one-dimensional optical lattice created from counter propagating laser beams (a) and with beams enclosing an angle  $\theta$  (b). The parameters  $V_0$  (lattice depth) and  $d$  (lattice spacing) are defined in the text. Figure taken from [33].

where  $\varepsilon_i$  is the on-site potential at each site  $i$  and  $k_{i,j}$  is the tunneling rate between adjacent sites  $i$  and  $j$ . The operators  $\hat{n}_i = \hat{b}_i^\dagger \hat{b}_i$  count the number of bosons at site  $i$ . The annihilation and creation operators,  $\hat{b}_i$  and  $\hat{b}_i^\dagger$ , obey the commutation relations  $[\hat{b}_i, \hat{b}_j^\dagger] = \delta_{i,j}$ . The on-site interaction strength is represented by  $U_i$ , which, due to the low temperatures necessary to achieve a Bose-Einstein Condensate, is governed predominantly by  $s$ -wave scattering. The Hamiltonian, Eq. (2.3), has two constants of motion: the energy  $E$  and the total number of particles  $N = \sum_{i=1}^s n_i$ . The interaction potential is often approximated to a delta function due to the inherent low particle density of the BEC [30]. In this approximation, the interatomic interaction strength is equal to

$$U_i = \frac{4\pi a_s \hbar^2}{m} \quad (2.4)$$

where  $a_s$  is the  $s$ -wave scattering and  $m$  is the mass of the particles.

Experimentally, all three parameters,  $\varepsilon$ ,  $U$ , and  $k$  can be controlled. For example, in optical lattices, the on-site potential is directly related to the intensity of the lasers used

to create the lattice potential [30]. The interaction strength can be modified by changing  $a_s$ . The  $s$ -wave scattering length can be adjusted to both negative and positive values by applying an external magnetic, optical, radio-frequency, or electric field [44]. Finally, the on-site potential can be regulated by changing the depth of the lattice sites [30].

## 2.4 The Classical Limit of the Bose-Hubbard Hamiltonian and the Discrete Nonlinear Schrödinger Equation

Interacting bosonic systems described by the BHH have a well-defined classical limit and these provide excellent models with which fundamental issues concerning quantum-classical correspondence (QCC) can be investigated, both theoretically and experimentally. Below we describe a method that will allow us to identify the classical limit of a BHH. To this end, we define new raising and lowering operators:

$$\hat{A}_i = \frac{1}{\sqrt{N}} \hat{b}_i; \quad \hat{A}_i^\dagger = \frac{1}{\sqrt{N}} \hat{b}_i^\dagger; \quad \hat{n}_i = \frac{1}{N} \hat{n}_i \quad (2.5)$$

With these new raising and lowering operators the BHH becomes

$$\frac{\hat{H}}{N} = \sum_{i=1}^s \varepsilon_i \hat{n}_i + \frac{N}{2} \sum_{i=1}^s U_i \hat{n}_i (\hat{n}_i - \frac{1}{N}) - \sum_{\langle i,j \rangle}^s k_{i,j} [\hat{A}_i^\dagger \hat{A}_j + \hat{A}_j^\dagger \hat{A}_i] \quad (2.6)$$

which is the energy per boson.

Assuming that the lattice is homogeneous, i.e. the interatomic interactions and the tunneling rates are the same for all sites ( $U_i = U$  and  $k_{i,j} = k$ ), we rewrite Eq. (2.6) such that  $\tilde{U}$  stays constant as  $N$  is changed. Now when we take the limit  $N \rightarrow \infty$ , our new Hamiltonian is<sup>2</sup>

$$\mathcal{H} = \frac{\hat{H}}{N} = \sum_{i=1}^s \varepsilon_i \hat{n}_i + \frac{\tilde{U}}{2} \sum_{i=1}^s \hat{n}_i \hat{n}_i - k \sum_{i,j}^s [\hat{A}_i^\dagger \hat{A}_j + \hat{A}_j^\dagger \hat{A}_i], \quad (2.7)$$

in which we have introduced the *effective nonlinearity*,  $\tilde{U}$ ,

---

<sup>2</sup>We now assume that we are working with a homogeneous lattice where  $U_i = U$  and  $k_{i,j} = k$ . If the lattice were heterogeneous, we could use  $\bar{k}$  and  $\bar{U}$ , the average values of  $U_i$  and  $k_{i,j}$ .

$$\tilde{U} = UN. \quad (2.8)$$

Next, we note that the commutation relation between  $\hat{A}_i$  and  $\hat{A}_i^\dagger$  goes to zero for large  $N$ , since

$$[\hat{A}_i, \hat{A}_i^\dagger] = \frac{1}{N} \delta_{i,j} \quad (2.9)$$

In fact, from Eq. (2.9), we can define an *effective*  $\hbar_{eff} = 1/N$ . Additionally, we note that since, in the limit  $N \rightarrow \infty$ , the right-hand side of Eq. (2.9) goes to zero,  $\hat{A}_i$  and  $\hat{A}_i^\dagger$  become c-numbers. In this classical limit, the quantum Hamiltonian (Eq. (2.7)) transforms into its classical counterpart:

$$\mathcal{H} = \sum_{i=1}^s \varepsilon_i |A_i|^2 + \frac{\tilde{U}}{2} \sum_{i=1}^s |A_i|^4 - k \sum_{i,j} [A_i^* A_{i-1} + A_{i-1}^* A_i]. \quad (2.10)$$

The Hamiltonian (Eq. (2.10)) describes a system of  $s$  nonlinear coupled oscillators. The generated dynamics is determined by the dimensionless ratio  $\lambda = k/\tilde{U}$ : For  $\lambda \rightarrow 0$  the interaction term dominates and the system behaves as a set of uncoupled oscillators while for  $\lambda \rightarrow \infty$  the kinetic term dominates. In both extremes, the classical dynamics are integrable. For intermediate values of  $\lambda$  (and for  $s > 2$ ) chaotic motion emerges. We thus conclude that the appropriate semiclassical limit is  $N \rightarrow \infty$  (i.e.  $\hbar_{eff} \rightarrow 0$ ), while simultaneously keeping  $\tilde{U}$  constant such that the underlying classical dynamics remain unchanged. The amplitudes  $A_i$  and  $A_i^*$  are conjugate variables with respect to the Hamiltonian,  $i\mathcal{H}$ . The resulting canonical equations of motion read:

$$i \frac{\partial A_l}{\partial t} = \frac{\partial \mathcal{H}}{\partial A_l^*}; \quad -i \frac{\partial A_l^*}{\partial t} = \frac{\partial \mathcal{H}}{\partial A_l}, \quad (2.11)$$

from which we can derive what is known as the discrete nonlinear Schrödinger (DNLS) equation

$$i\dot{A}_l = \varepsilon_l A_l + \tilde{U}|A_l|^2 A_l - k(A_{l-1} + A_{l+1}). \quad (2.12)$$

The DNLS equation will allow us to solve for  $A_l$  associated with the lattice potential, therefore providing a means to compare and contrast the quantum and classical observables for the system. This will be done for the dimer in the following two chapters.

## 2.5 The Bose-Hubbard Hamiltonian in Fock-space

The wave function associated with bosons trapped in a lattice potential is most easily represented in Fock-space. The total number of particles,  $N$ , is

$$N = \sum_{i=1}^s n_i. \quad (2.13)$$

$N$  is a constant of motion, both in the quantum and classical limits. This can be seen for the quantum case by calculating the commutation relation between the BHH (Eq. (2.3)) and the total number of particles (Eq. (2.13)). Specifically, we find<sup>3</sup>

$$\frac{\partial N}{\partial t} = \frac{i}{\hbar} \langle [\hat{H}, N] \rangle = 0. \quad (2.14)$$

In the classical limit, the Poisson bracket of the classical Hamiltonian (Eq. (2.7)) and the total number particles is  $\frac{\partial N}{\partial t} = \{\mathcal{H}, N\} = 0$ . Hence, also in the classical limit, the total number of particles in the system is conserved.

By using the Fock number states,  $|n_1, n_2, \dots, n_i, \dots, n_s \rangle$ , as a basis, we can easily describe the number of atoms,  $n_i$ , at each site using any of the vectors spanned in the Fock-space

$$\{ \underbrace{|N, 0, \dots, 0 \rangle}_{s \text{ terms}}, |N-1, 1, \dots, 0 \rangle, |N-1, 0, 1, 0, \dots, 0 \rangle, \dots, |N-1, 0, \dots, 0, 1 \rangle, |N-2, 2, 0, \dots, 0 \rangle, \\ |N-2, 1, 1, 0, \dots, 0 \rangle, \dots, |N-2, 0, \dots, 2 \rangle, \dots, |0, \dots, 0, N \rangle \} \quad (2.15)$$

The raising and lowering operators act as such on the wave functions:

---

<sup>3</sup>See Appendix A for a proof.

$$\hat{b}_i |n_1, n_2, \dots, n_i, \dots, n_s \rangle = \sqrt{n_i} |n_1, n_2, \dots, n_i - 1, \dots, n_s \rangle \quad (2.16)$$

$$\hat{b}_i^\dagger |n_1, n_2, \dots, n_i, \dots, n_s \rangle = \sqrt{n_i + 1} |n_1, n_2, \dots, n_i + 1, \dots, n_s \rangle \quad (2.17)$$

One can then use this basis in order to write the BHH (Eq. (2.3)). The dimension of our Hilbert space,  $\mathcal{N}$ , is defined by the number of different ways our  $N$  indistinguishable bosons can be distributed among the  $s$  different wells [4]

$$\mathcal{N} = \frac{(N + s - 1)!}{N!(s - 1)!}. \quad (2.18)$$

## 2.6 Applications of the Bose-Hubbard Hamiltonian and the DNLS

Though a large portion of the current literature on the BHH and the DNLS centers around BEC, these mathematical models have applications in a variety of different physical systems.

One of these systems is the Josephson Junctions array (JJA), shown in Fig. 2.4a. A JJA is made up of a series of Josephson Junctions (JJ) in various geometric configurations. Josephson Junctions are formed by two coupled macroscopic quantum fluids. Josephson Junction Arrays allow for the study of quantum phase transitions and phase coherence, which is an important part of developing quantum computer schemes. Previous to the realization of the BEC in 1995, there were a limited number of geometric configurations in which the JJA could be studied. Using the BEC allows for more precise control of the parameters of the array and thus makes a variety of geometric configurations which were previously inaccessible possible to achieve [7]. While the experiments which center around BECs are performed with neutral atoms with integer spins, JJA experiments are done with charged bosons, which are formed by Cooper pairs of electrons. Thus, the on-site interaction strength,  $U_i$ , is dominated by Coulomb forces, rather than  $s$ -wave interactions. Additionally, the coupling term,  $k_{i,j}$ , is defined by the Josephson energy,

$E_J$  [24]. Various phenomena have been observed using JJA, including superconducting-insulator transitions or Josephson oscillations [17].

Furthermore, the BHH and the DNLS equation are also used to describe the vibrational part of the bond excitations of small molecules [40] and biological polymers [18]. These systems have both been studied in the classical limit [14] as well as the quantum [8, 11, 37, 49]. Analogous to a spring constant, the coupling term,  $k_{i,j}$ , represents both the electromagnetic and the mechanical coupling of adjacent atoms. On the other hand, the nonlinearity,  $U_i$ , specifies the anharmonic softening of bonds under stress [24]. The BHH also applies to the behavior of coupled nonlinear microscopic cantilevers, as shown in Fig. 2.4b. Arrays of micro-cantilevers have been used to identify and select biomolecules[19].

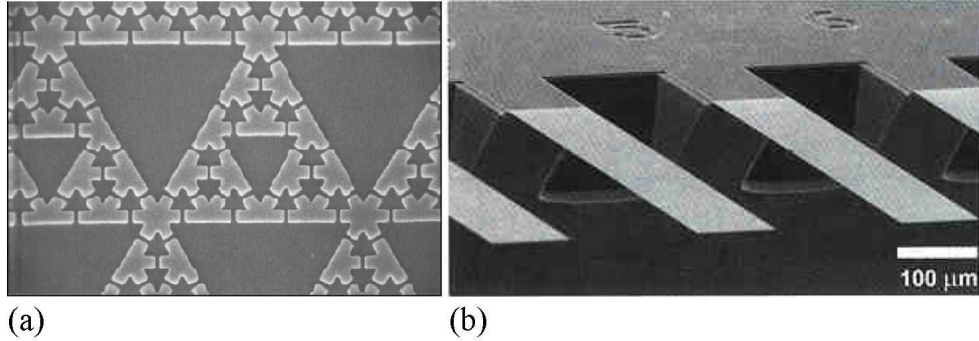


Figure 2.4: Two different physical system which both can be described using the BHH or DNLS. (a) Coupled Josephson Junctions with the geometry of periodically repeated Sierpinski gaskets, superconducting metal is Pb (clear) while the normal metal is Cu (dark). Taken from [23]. (b) Scanning electron micrograph of a section of a microfabricated silicon cantilever array (eight cantilevers, each  $1 \mu m$  thick,  $500 \mu m$  long, and  $100 \mu m$  wide, with a pitch of  $250 \mu m$ , spring constant  $0.02 N/m$ ; Micro- and Nanomechanics Group, IBM, Zurich Research Laboratory, Switzerland). Taken from [19].

# 3 Bose-Einstein Condensate trapped in a double-well potential: Stationary States

A vital step towards understanding the dynamics generated by the BHH is to understand its stationary properties, i.e. its eigenvalues and corresponding eigenfunctions. Thus, in this chapter we will compare the stationary solutions of the quantum Bose-Hubbard Hamiltonian to the those generated from classical Hamiltonian for the dimer.

This chapter is structured in the following way: In §3.1, we derive the BHH matrix for the dimer in Fock-space, which we use to numerically calculate the quantum energy levels and eigenstates of the dimer. Then, in §3.2, we use the DNLS equation to derive the energies for the classical limit of the dimer and compare them to those calculated in §3.1. Finally, in §3.3, we explore the small coupling strength regime and the small interatomic interaction regime via quantum mechanical perturbation theory and derive expressions for the eigenvalues and eigenvectors of the quantum dimer.

## 3.1 Bose-Hubbard Dimer

For a two site lattice, the Bose-Hubbard Hamiltonian (Eq. (2.3)) becomes

$$\hat{H} = \varepsilon_1 \hat{n}_1 + \varepsilon_2 \hat{n}_2 + \frac{U_1}{2} \hat{n}_1(\hat{n}_1 - 1) + \frac{U_2}{2} \hat{n}_2(\hat{n}_2 - 1) - k(\hat{b}_1^\dagger \hat{b}_2 + \hat{b}_2^\dagger \hat{b}_1) \quad (3.1)$$

where, for sake of simplicity, we have relabeled  $k_{12}$  as in Eq. (2.3) with  $k$ .

In order to do numerical calculations of the state vectors for the quantum BHH, we

### 3 Bose-Einstein Condensate trapped in a double-well potential: Stationary States

need to derive the matrix form of the Hamiltonian. To achieve this, we sandwich Eq. (3.1) between two different state vectors,  $\langle m|\hat{H}|n\rangle$  where  $m, n \in \mathbb{Z}$  and run from 1 to  $\mathcal{N} = N + 1$ . Since the number of particles,  $N$ , is conserved, for simplicity we have defined our vectors as  $|n_1\rangle \equiv |n_1, n_2\rangle \equiv |n_1, N - n_1\rangle$ . For the dimer, the Hamiltonian matrix in the Fock space reads:

$$\begin{aligned} \langle n_1|\hat{H}|n_2\rangle = & [\varepsilon_1 n_1 + \varepsilon_2 n_2 + \frac{U_1}{2}(n_1^2 - n_1) + \frac{U_2}{2}(n_2^2 - n_2)]\delta_{n_1, n_2} \\ & - k\sqrt{n_1(n_2 + 1)}\delta_{n_1, n_2+1} - k\sqrt{n_2(n_1 + 1)}\delta_{n_1, n_2-1} \end{aligned} \quad (3.2)$$

In Fig. 3.1, based on Ref. [25], the calculations for the energy levels of a system of twenty-nine particles is shown. In the limit of small coupling strength, the energy levels are doubly degenerate. As the coupling strength is increased, the degeneracy is lifted, beginning from the lower energy levels until the levels bifurcate into thirty, i.e.  $N + 1$ , energy levels. In the following sections, we will be discussing the structure of the energy levels using two approaches: (a) semi-classical analysis based on the DNLS equation and (b) quantum mechanical perturbation theory with respect to the nonlinear interaction and the coupling strength.

## 3.2 Classical Stationary States

In the previous chapter, we discussed the semiclassical limit of the BHH, the DNLS equation (Eq. (2.12)). In the next step, we compare the quantum energy levels found numerically in §3.1 (see Fig. 3.1) to the classical energies for the stationary state scenario.

We define the classical stationary solutions as

$$A_j = \phi_j e^{i\omega t}, \quad (3.3)$$

where  $\phi_j$  is real and where  $\sum_j |A_j|^2 = N$ . By substituting Eq. (3.3) into Eq. (2.12), we find

$$\omega\phi_l + \varepsilon_l\phi_l + \tilde{U}\phi_l^2\phi_l - k(\phi_{l-1} + \phi_{l+1}) = 0, \quad (3.4)$$

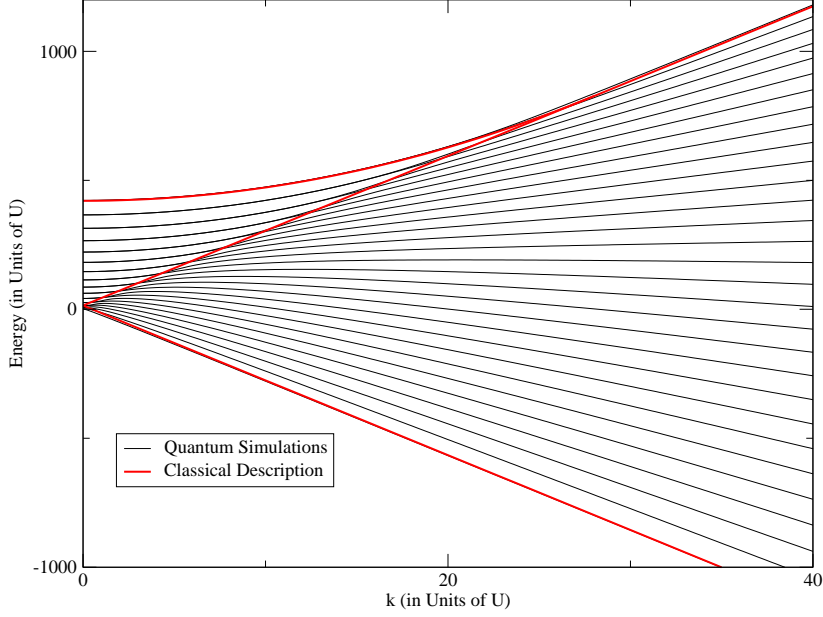


Figure 3.1: The energies obtained for the Bose-Einstein Condensate in a double-well potential. The on-site potentials  $\varepsilon_1 = \varepsilon_2 = 0$ , the interatomic interaction strengths  $U_1 = U_2 = U$ , and  $N = 29$ . The black lines represent the numerically obtained quantum energy levels. The red lines are the over-plotted classical solutions as derived in §3.2.

from which, for the specific case of the dimer, we get the following set of equations:

$$\begin{aligned} \omega\phi_1 + \tilde{U}\phi_1^2\phi_1 - k\phi_2 &= 0 & (a) \\ \omega\phi_2 + \tilde{U}\phi_2^2\phi_2 - k\phi_1 &= 0 & (b) \\ \phi_1^2 + \phi_2^2 &= N & (c) \end{aligned} \tag{3.5}$$

By multiplying Eq. (3.5a) by  $\phi_2$  and Eq. (3.5b) by  $\phi_1$  and subtracting, we find:

$$-\tilde{U}\phi_1\phi_2(\phi_1^2 - \phi_2^2) + k(\phi_2^2 - \phi_1^2) = 0 \tag{3.6}$$

Thus,

$$\phi_1 = \pm\phi_2 \tag{3.7}$$

and, assuming  $\phi_1, \phi_2 \neq 0$ ,

$$\phi_2 = -\frac{k}{\tilde{U}\phi_1}. \tag{3.8}$$

By substituting this equation into Eq. (3.5c), we obtain the asymmetric solution

$$\phi_1 = \sqrt{\frac{N + \sqrt{N^2 - 4\frac{k^2}{\tilde{U}^2}}}{2}}; \quad \phi_2 = \sqrt{\frac{N - \sqrt{N^2 - 4\frac{k^2}{\tilde{U}^2}}}{2}}, \quad (3.9)$$

while for the case of Eq. (3.7), we find the symmetric and antisymmetric solutions

$$\phi_1 = \pm\phi_2 = \pm\sqrt{\frac{N}{2}}. \quad (3.10)$$

When substituted into the classical Hamiltonian, Eq. (3.4), the energies corresponding to the stationary solutions can be derived. The energy associated with Eq. (3.9) is

$$\mathcal{H} = \frac{\tilde{U}N^2}{2} + \frac{k^2}{\tilde{U}}. \quad (3.11)$$

while for  $\phi_1 = \pm\phi_2$ , the energy is

$$\mathcal{H} = \frac{\tilde{U}N^2}{4} \mp kN \quad (3.12)$$

The energies in Eqs. (3.11) and (3.12) when plotted over the quantum energy levels as in Fig. 3.1 create an enveloping function for the quantum energy levels.

### 3.3 Quantum Mechanical Perturbation Theory

In this section, we analyze the stationary properties of the dimer BHH. Using perturbation theory we compare our results with the classical calculations of §3.2 and the numerical results of §3.1. In §3.3.1, we present the perturbation theory for the small coupling regime, i.e.  $k \ll U$ . Similarly, we the perturbation theory for the small interatomic interaction regime, i.e.  $U \ll k$ , is derived in §3.3.2.

#### 3.3.1 Small coupling regime

In the small coupling regime, we do time-independent perturbation theory on a Hamiltonian,  $H_0$ , which describes the uncoupled double well system:

$$H_0 = \frac{U}{2} \left[ b_1^\dagger b_1 (b_1^\dagger b_1 - 1) + b_2^\dagger b_2 (b_2^\dagger b_2 - 1) \right], \quad (3.13)$$

### 3 Bose-Einstein Condensate trapped in a double-well potential: Stationary States

where without loss of generality we assume that  $\varepsilon_1 = \varepsilon_2 = 0$  and  $U_1 = U_2$  as in Fig. 3.1. The perturbing Hamiltonian,  $H'$ , as defined by the intra-well coupling is

$$H' = b_1^\dagger b_2 + b_2^\dagger b_1, \quad (3.14)$$

thus our full Hamiltonian is

$$H = H_0 - kH' \quad (3.15)$$

The small coupling regime stationary state solutions call for a distinction between the cases where the number of particles,  $N$ , is even and where it is odd.

#### Case 1: Even $N$

The ground state corresponds to an equidistribution of the particles and for an even number of particles has the trivial first-order correction:

$$E_0^{(1)} = \langle \frac{N}{2} | H' | \frac{N}{2} \rangle = 0. \quad (3.16)$$

The second-order correction to the ground state is

$$E_0^{(2)} = \sum_{n_1=0}^N \frac{|\langle n_1 | H' | \frac{N}{2} \rangle|^2}{E_0^{(0)} - E_{n_1}^{(0)}} \quad (3.17)$$

where the degenerate eigenvalues for  $k = 0$  is  $E_{n_1}^{(0)} = n_1^2 - Nn_1 - N/2 + N^2/2$ . Thus,

$$E_0^{(2)} = -k^2 \frac{N}{2} \left( \frac{N}{2} + 1 \right). \quad (3.18)$$

The first-order correction for the excited states is

$$E_{n_1}^{(1)} = \langle n_1 | H' | N - n_1 \rangle = 0 \quad (3.19)$$

because for even  $N$ , the population difference between two degenerate states will never be less than two bosons. Therefore, the coupling in first order, which only transfers one

### 3 Bose-Einstein Condensate trapped in a double-well potential: Stationary States

boson at a time, will never make  $|n_1 \rangle \equiv |n_1, N - n_1 \rangle$  and  $|N - n_1 \rangle \equiv |N - n_1, n_1 \rangle$  equal. Using degenerate perturbation theory, the second-order correction to the excited states is calculated from the perturbation matrix [25]

$$W_{n'_1, n''_1} = \sum_{l \neq n_1, N - n_1}^N \frac{\langle n'_1 | H' | l \rangle \langle l | H' | n''_1 \rangle}{E_{n_1}^{(0)} - E_l^{(0)}}. \quad (3.20)$$

When  $l \neq N/2 + 1, N/2 - 1, N/2$ ,  $W$  only has diagonal elements

$$W_{\frac{N}{2}+1, \frac{N}{2}+1} = W_{\frac{N}{2}-1, \frac{N}{2}-1} = k^2 \frac{N^2 + N - 2Nn_1 + 2n_1^2}{2[(N - 2n_1)^2 - 1]}. \quad (3.21)$$

For the cases where  $l = N/2 + 1, N/2 - 1$ , the perturbation matrix becomes

$$W = k^2 \begin{bmatrix} \frac{N}{6}(\frac{N}{2} + 1) + 1 & \frac{N}{4}(\frac{N}{2} + 1) \\ \frac{N}{4}(\frac{N}{2} + 1) & \frac{N}{6}(\frac{N}{2} + 1) + 1 \end{bmatrix} \quad (3.22)$$

from which we can calculate the second order energy corrections to the first excited state

$$E_{\pm}^{(2)} = k^2 \left[ \frac{N}{6} \left( \frac{N}{2} + 1 \right) + 1 \pm \frac{N}{4} \left( \frac{N}{2} + 1 \right) \right] \quad (3.23)$$

The 0th order eigenvectors for the first excited states is given by

$$|\psi_{\pm}^{(0)}(l) \rangle = \alpha \left| \frac{N}{2} - l \right\rangle \pm \beta \left| \frac{N}{2} + l \right\rangle, \quad (3.24)$$

where  $\alpha$  and  $\beta$  are the coefficients which form the eigenvectors of  $W$  (Eq. (3.22)). Thus, the 0th order eigenvectors for the first excited states are

$$|\psi_{\pm}^{(0)}(1) \rangle = \frac{1}{\sqrt{2}} \left( \left| \frac{N}{2} - 1 \right\rangle \pm \left| \frac{N}{2} + 1 \right\rangle \right) \quad (3.25)$$

Analogously, the eigenvectors of our Hamiltonian, Eq. (3.15), following the work of Ref. [25], are given to second order as

$$\begin{aligned} |h_{r_{\pm}} \rangle = & X_r |r_{\pm} \rangle + Y_r^+ |(r+1)_{\pm} \rangle + Y_r^- |(r-1)_{\pm} \rangle \\ & + Z_r^+ |(r+2)_{\pm} \rangle + Z_r^- |(r-2)_{\pm} \rangle, \end{aligned} \quad (3.26)$$

### 3 Bose-Einstein Condensate trapped in a double-well potential: Stationary States

where  $n = N/2 - r$  with  $r \neq 0, 1, \frac{1}{2}$  and

$$\begin{aligned} X_r(k) &= 1 - \frac{k^2}{4} \frac{4J^2 r^2 + J^2 - 4r^4 + 3r^2}{(4r^2 - 1)^2} \\ Y_r^\pm(k) &= \pm \frac{k}{2} \frac{\sqrt{J^2 - r(r \pm 1)}}{2r \pm 1} \\ Z_r^\pm(k) &= \frac{k^2}{16} \frac{\sqrt{[J^2 - r(r \pm 1)][J^2 - (r \pm 1)(r \pm 2)]}}{(r \pm 1)(2r \pm 1)} \end{aligned} \quad (3.27)$$

The three special cases where  $r = 0, 1, \frac{1}{2}$ , correspond to the ground state and first and second excited states of the even  $N$  case and the ground state of the odd  $N$  case (see §Case 2: Odd  $N$ ). The ground state to second order is

$$|h_0 \rangle = \left(1 - \frac{k^2 J^2}{4}\right) |\psi^{(0)}(0) \rangle + k \sqrt{\frac{J^2}{2}} |\psi_+^{(0)}(1) \rangle + \frac{k^2}{8} \sqrt{\frac{J^2(J^2 - 2)}{2}} |\psi_+^{(0)}(2) \rangle, \quad (3.28)$$

the first excited state is

$$\begin{aligned} |h_{1-} \rangle = & \left(1 - \frac{k^2}{72}(19J^2 - 2)\right) |\psi_-^{(0)}(1) \rangle + \frac{k}{6} \sqrt{J^2 - 2} |\psi_-^{(0)}(2) \rangle \\ & + \frac{k^2}{96} \sqrt{(J^2 - 6)(J^2 - 2)} |\psi_-^{(0)}(3) \rangle, \end{aligned}$$

and the second excited state is

$$\begin{aligned} |h_{1+} \rangle = & \left(1 - \frac{k^2}{72}(19J^2 - 2)\right) |\psi_+^{(0)}(1) \rangle + \frac{k}{6} \sqrt{J^2 - 2} |\psi_+^{(0)}(2) \rangle \\ & + \frac{k^2}{96} \sqrt{(J^2 - 6)(J^2 - 2)} |\psi_+^{(0)}(3) \rangle - k \sqrt{\frac{J^2}{2}} |\psi^{(0)}(0) \rangle. \end{aligned}$$

The general energy corrections to second order to the remaining degenerate states are found from the perturbation matrix as given in Eq. (3.21) to be

$$E_{|\frac{N}{2} \pm l \rangle} = 2 \left(\frac{N}{2} \pm l\right)^2 + k^2 \frac{\frac{N}{2} \left(\frac{N}{2} + 1\right) + \left(\frac{N}{2} \pm l\right)^2}{4 \left(\frac{N}{2} \pm l\right)^2 - 1}, \quad (3.29)$$

where  $l$  is an integer.

#### Case 2: Odd $N$

In the case that  $N$  is odd, all states are degenerate, including the ground state. Following similar steps as in Eq. (3.17), we find that the first order energy corrections for the doubly degenerate ground state are

$$E_{|\frac{N+1}{2}\rangle}^{(1)} = k\frac{N+1}{2}; \quad E_{|\frac{N-1}{2}\rangle}^{(1)} = -k\frac{N+1}{2}, \quad (3.30)$$

from which we can derive the 0th order eigenvectors

$$|\psi_{\pm}^{(0)}\rangle = \frac{1}{\sqrt{2}} \left( \left| \frac{N-1}{2} \right\rangle \pm \left| \frac{N+1}{2} \right\rangle \right). \quad (3.31)$$

The ground state to second order is

$$\begin{aligned} |h_{1/2\pm}\rangle = & \left( 1 - \frac{k^2}{32} \left[ J^2 - \frac{3}{4} \right] \right) |\psi_{\pm}^{(0)}(\frac{1}{2})\rangle + \left[ \frac{k}{4} \sqrt{J^2 - \frac{3}{4}} \mp \frac{k^2}{16} \sqrt{\left( J^2 + \frac{1}{4} \right) \left( J^2 - \frac{3}{4} \right)} \right] |\psi_{\pm}^{(0)}(\frac{3}{2})\rangle \\ & + \frac{k^2}{48} \sqrt{\left( J^2 - \frac{3}{4} \right) \left( J^2 - \frac{15}{4} \right)} |\psi_{\pm}^{(0)}(\frac{5}{2})\rangle \end{aligned} \quad (3.32)$$

while the rest of the states are given to second order by Eq. (3.26). The second order energy correction for both  $|\frac{N+1}{2}, \frac{N-1}{2}\rangle$  and  $|\frac{N-1}{2}, \frac{N+1}{2}\rangle$  is

$$E_0^{(2)} = -k^2 \frac{N^2 + 2N - 3}{16}. \quad (3.33)$$

Analogously, the first excited state has the same energy corrections as the system with an even number of bosons, as shown in Eqs. (3.19) and (3.23). The energy corrections to second order of the remaining states are the same as those in Eq. (3.29), where  $l$  is a half-integer.

The above expressions make it clear that the lower level perturbative corrections appear as a combination of the perturbative parameter,  $k$ , with the total number of bosons,  $N$ . This combination depends on the particular energy level. For the lower levels (see Eqs. (3.18) and (3.33)) the perturbative corrections appear as the product  $kN$ , indicating that, as the boson population grows, the perturbation theory holds true for ever shrinking values of  $k$ . On other hand, for the higher energy levels the perturbative corrections appear as a decreasing function of the number of bosons (see Eq. (3.29)), thus the perturbative results remain accurate to large values of  $k$ . These conclusions are confirmed in Fig. 3.2, where we compare the numerical results for the eigenvalues of the BHH with the perturbative expressions derived in this section. For higher levels one can

see that the agreement with the perturbative expressions persist for larger values of  $k$ .

### 3.3.2 Small interatomic interaction regime<sup>1</sup>

In the weak interatomic interaction regime, it is simpler to approach the perturbation theory using the angular momentum representation of the BHH [43]. We now turn to the weak interatomic interaction regime. Here it is important to remember that the total number operator,  $\hat{N} = \hat{n}_1 + \hat{n}_2$ , is a constant of motion and is equal to the total number of atoms,  $N$ . We now define the following three operators which obey SU(2) commutation relations,

$$J_x = \frac{1}{2}(\hat{b}_1^\dagger \hat{b}_2 + \hat{b}_2^\dagger \hat{b}_1), \quad J_y = \frac{i}{2}(\hat{b}_1^\dagger \hat{b}_2 - \hat{b}_2^\dagger \hat{b}_1), \quad J_z = \frac{1}{2}(\hat{b}_2^\dagger \hat{b}_2 - \hat{b}_1^\dagger \hat{b}_1). \quad (3.34)$$

The Casimir invariant is trivially found to be

$$J^2 = \frac{N}{2} \left( \frac{N}{2} + 1 \right). \quad (3.35)$$

This is analogous to an angular momentum model in which the total angular momentum given by  $j = N/2$ .

The operator  $J_x$  corresponds to the particle occupation number imbalance between the single-particle energy eigenstates. For example, the maximal weight eigenstate  $|j, j\rangle_z$  corresponds to all the particles occupying the highest single-particle energy eigenstate. The operator  $J_z$  gives the particle number difference between the localized states of each well. Its maximal and minimal weight eigenstates correspond to the localization of all the particles in either of the wells. Finally, the operator  $J_y$  is crucial to an understanding of tunneling, since it represents the condensate momentum.

In this representation, the dimer Hamiltonian (Eq. (3.1)) (for  $U_i = U$  and  $k_{i,j} = k$ ) may be written as

$$H = H_0 + \frac{U}{2} H' \quad (3.36)$$

---

<sup>1</sup>An expanded version with more detailed algebra can be found in Appendix B.

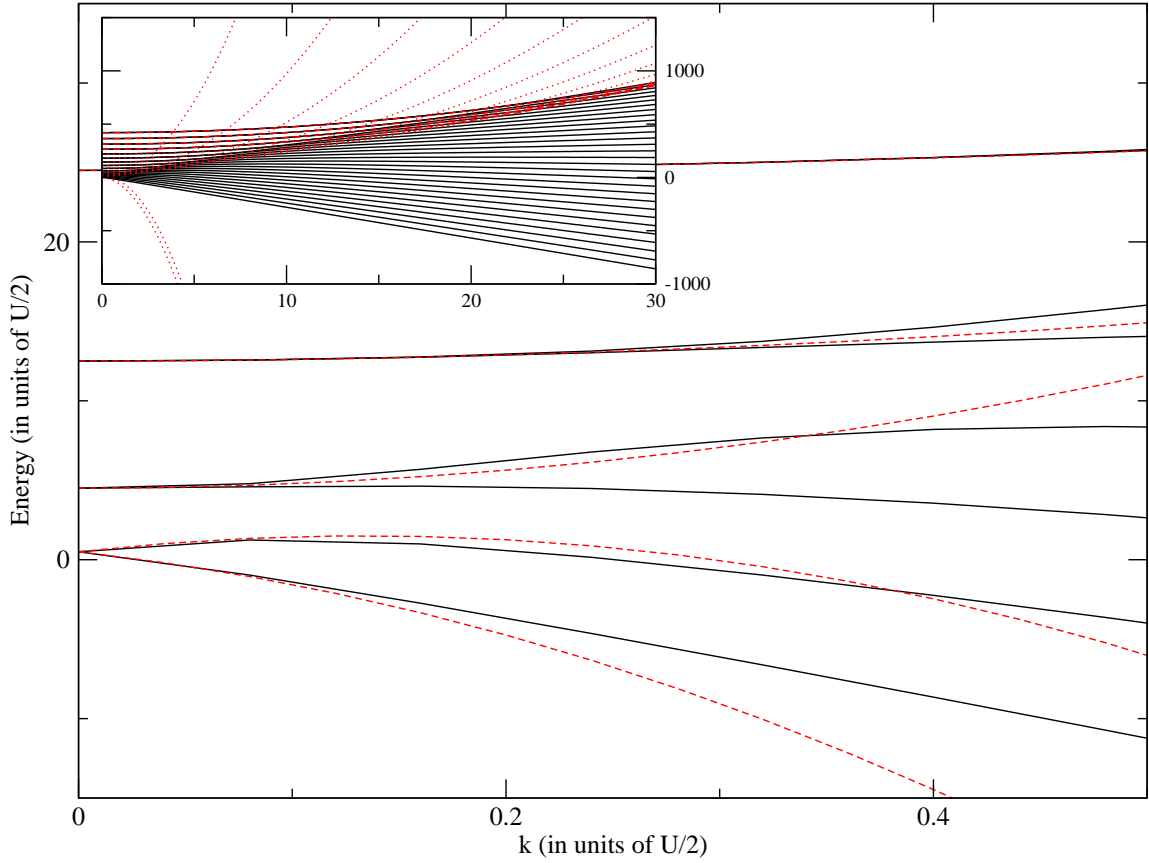


Figure 3.2: Energy levels of the dimer BHH in the weak coupling regime. The black lines are the exact energies, while the red dotted and dashed lines are the energy levels obtained from second order perturbation theory. We note that highest energies (dashed lines) match well for the first thirty units of  $k$ . The inset shows the the good fitting of the perturbation theory for the higher energy levels of the dimer BHH. Here it is evident that up to second order, only the singular ground state is split, while the rest of the energy levels remain degenerate.

where

$$H_0 = -2kJ_x, \quad (3.37)$$

while the perturbing Hamiltonian is

$$H' = \frac{N^2}{2} - N + 2J_z^2. \quad (3.38)$$

The Hamiltonian (Eq. (3.36)) describes a linear precession about the  $x$ -axis at the tunneling frequency and a nonlinear precession about the  $z$ -axis at a rate determined by the value of the  $z$ -component of the angular momentum.<sup>2</sup> In order to use the small interatomic interaction perturbation theory, we need to move to the  $J_x$ -basis. Thus, we need to convert the vectors used to span the Fock-state as described in §2.5 into the  $J_x$ -basis. An arbitrary vector in the  $J_x$ -basis can be written as a superposition of the eigenstates of the  $J_z$ -basis via the relationship

$$|j, m \rangle_x = \sum_{n=-j}^j A_n^{(m)} |j, n \rangle_z, \quad (3.39)$$

where

$$A_n^{(m)} = 2^n \left[ \frac{(j+n)!(j-n)!}{(j+m)!(j-m)!} \right]^{1/2} P_{j+n}^{(m-n, -m-n)}(0). \quad (3.40)$$

$P_n^{(\alpha, \beta)}(z)$  is the Rodriguez formula for Jacobi polynomials (see Appendix B).

The 0th order energy is

$$E_n^{(0)} = {}_x \langle n | H_0 | n \rangle_x = -2kn \quad (3.41)$$

The first order energy corrections are given by standard perturbation theory to be

$$\begin{aligned} E_n^{(1)} &= {}_x \langle n | H' | n \rangle_x \\ &= \sum_m |A_m^{(n)}|^2 m^2. \end{aligned} \quad (3.42)$$

In Fig. 3.3, we compare the results for the eigenvalues of the first order perturbation

---

<sup>2</sup>It is interesting to note that the Hamiltonian (Eq. (3.36)) looks similar to the nonlinear top models considered by Haake [20].

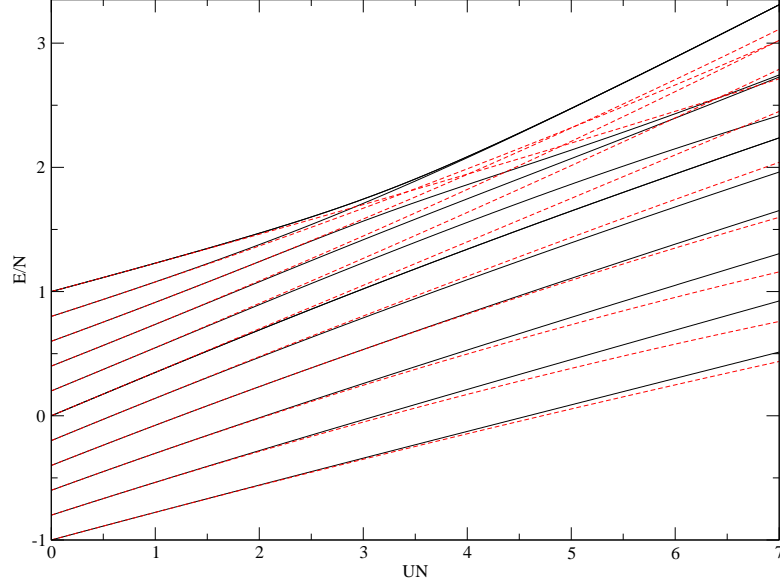


Figure 3.3: The second order energy level corrections (red) in the small interatomic interaction regime overplotted on the exact energy levels (black) for 10 particles, where  $k = 1$ .

theory, Eq. (3.42), with the exact eigenvalues extracted by direct diagonalization of Eq. (3.1). As one can see, the agreement is quite good up to the values of  $\tilde{U}$  where the energy level degeneracy occurs. This agreement is better for the lower part of the spectrum than the upper energies indicating that the perturbation theory expansion converges with a different rate for various parts of the spectrum. This can be seen more clearly in Fig. 3.4, where the wave function components (up to first order in the perturbation theory) are plotted versus the results of the exact diagonalization. The first order corrections in this case are given by the expression:

$$\begin{aligned}
 \psi_n^{(1)} &= \sum_{m \neq n} \frac{\langle \psi_m^{(0)} | H' | \psi_n^{(0)} \rangle}{E_n^{(0)} - E_m^{(0)}} \psi_m^{(0)} \\
 &= \sum_{m \neq n, l, r} \frac{A_l^{(n)} A_l^{(m)*} l^2}{-2k(m-n)} A_r^{(m)} |r\rangle_z .
 \end{aligned} \tag{3.43}$$

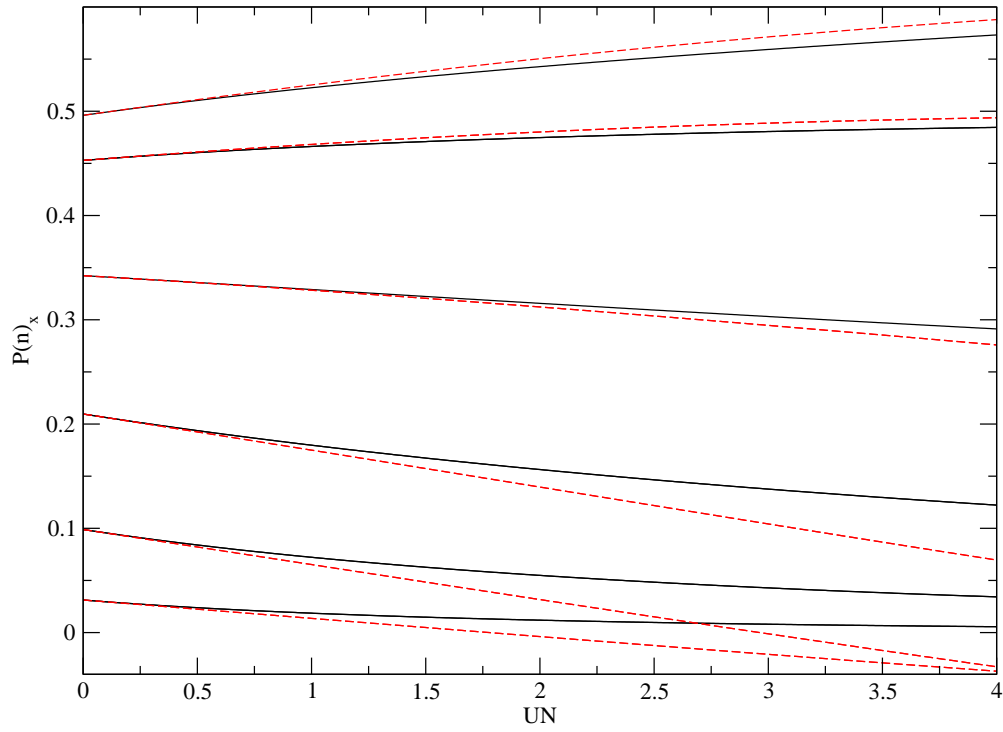


Figure 3.4: The components of the wave functions in the  $J_x$ -basis for 10 particles and  $k = 1$ . The black lines are the exact values, while the red lines are the first order wave functions from the small interatomic interaction perturbation theory.

## 4 Dynamics of the dimer

This chapter is dedicated to investigating the dynamical properties of a BEC trapped in a deep double well potential (dimer). We begin by summarizing a recent experiment performed by the Heidelberg group and discuss its importance to our work. Following the same structure as in Chapter 3, we will explore the dynamics generated by the DNLS equation, which describes the classical limit of the BHH. Three distinct dynamical regions are discovered: Josephson oscillations, self-trapping regime, and critical dynamics (the transition between the first two regimes). We will explain the characteristics of these regimes, including the necessary conditions to achieve these dynamics. Then we approach the quantum dynamics and investigate the evolution of the atomic population in the presence of interatomic interactions. First, we will probe the deviations in the atomic population evolution from the zero interatomic interaction case by direct numerical investigation, after which we will employ time-dependent perturbation theory and identify the limits of its validity. The chapter ends with a semiclassical calculation, which captures the essential features of the quantum dynamics in all three dynamical regimes.

### 4.1 The Heidelberg Experiment

One of the first, and fundamental, textbook examples highlighting the differences between quantum and classical mechanics is the tunneling of a quantum particle through a potential barrier. It demonstrates the manifestation of the wave nature of matter. Experimentally, such processes can be studied on a mesoscopic level. Among the various experiments in which quantum mechanical tunneling has been observed, the very recent

#### 4 Dynamics of the dimer

work of the Heidelberg group on the Josephson effect between two weakly coupled atomic Bose-Einstein condensates in a macroscopic double-well potential is especially relevant to this thesis [1].

Although Josephson junctions have been realized in other experimental set-ups, such as superconductors separated by a thin insulator [31] or in super fluid helium stored in two reservoirs connected by nanoscopic apertures [36, 45], Oberthaler's system was the first in which the nonlinear interatomic interactions played an essential role in the dynamics. The nonlinearity revealed new dynamical behaviors: when the atom population imbalance between the two wells was below a critical value, Josephson oscillations were predicted and observed, as in Fig. 4.1a; while when the population imbalance was above the critical value, the Josephson oscillations were hindered, and thus self-trapping behavior were anticipated and realized, as shown in Fig. 4.1b.

In this experiment the Heidelberg group used a  $^{87}\text{Rb}$  BEC. Laser cooling techniques as discussed in §2.2 were used with 811 nm wavelength lasers to achieve a BEC of  $1150 \pm 150$  atoms in a double-well potential with final trap frequencies of  $\omega_x = 2\pi \times 90(1)\text{Hz}$ ,  $\omega_y = 2\pi \times 66(1)\text{Hz}$ , and  $\omega_z = 2\pi \times 90(1)\text{Hz}$  (which give the harmonic oscillation frequency of an atom trapped inside the lattice well). Gravity is acting in the  $y$ -direction. The lasers were then adjusted to increase the depth of the wells in the  $x$ -direction to  $2\pi \times 412(20)\text{Hz}$  and were crossed at a relative angle of  $9^\circ$  so that their interference pattern would create a periodic potential with strong harmonic confinement, thus producing an effective double-well potential with a barrier height of  $2\pi \times 263(20)\text{Hz}$  and a separation of  $4.4(2)\ \mu\text{m}$  as in Fig. 4.1.

The initial preparation of the population imbalance is achieved by shifting the relative angle of the laser which determines the harmonic confinement in the  $x$ -direction via a piezo actuated mirror mount to create an asymmetrical potential. The BEC is then loaded into the asymmetrical double well and the laser is adjusted to recreate a symmetrical potential. Since the BEC will seek the lowest possible energy, the larger the degree of asymmetry of the double well, the higher the population will be in the lower well. Thus, a greater degree of asymmetry is used to achieve self-trapping than to realize Josephson oscillations (see top frames of Fig. 4.1). To initiate Josephson os-

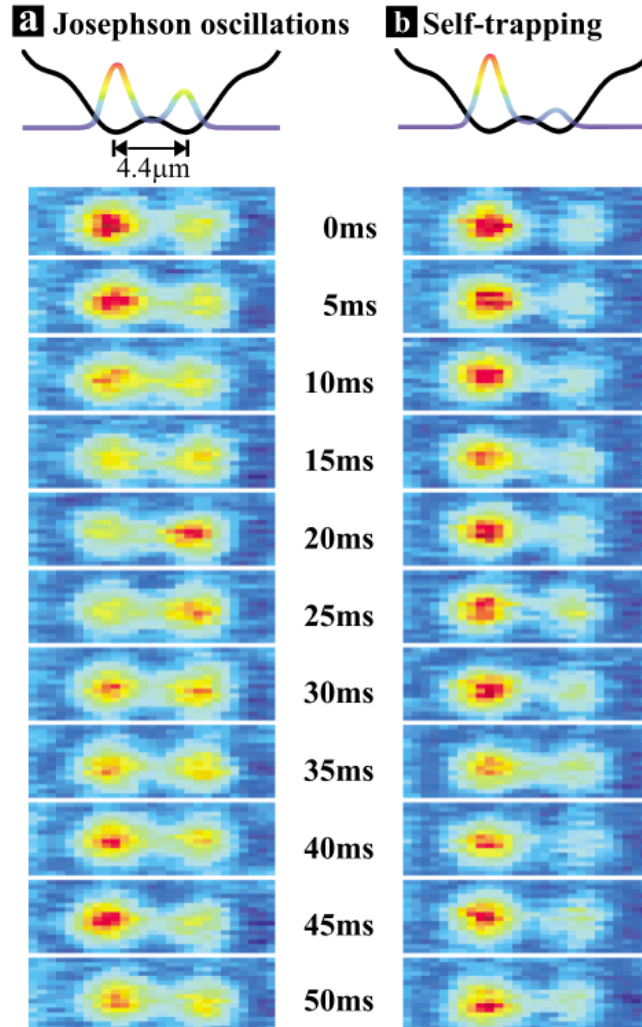


Figure 4.1: Observation of tunneling dynamics of two weakly linked Bose-Einstein condensates in a symmetric double-well potential as indicated in the schematics. The time evolution of the population of the left and right potential well is directly visible in the absorption images ( $19.4 \mu\text{m} \times 10.2 \mu\text{m}$ ). The distance between the two wave packets is increased to  $6.7 \mu\text{m}$  for imaging. (a) Josephson oscillations are observed when the initial population difference is chosen to be below the critical value  $z_c$ . (b) In the case of an initial population difference greater than the critical value the population in the potential minima is nearly stationary. This phenomenon is known as macroscopic quantum self-trapping. Figure taken from [1].

cillations, the asymmetrical double well is nonadiabatically converted to a symmetrical double well potential, so that the commencement of dynamics before the double well has been symmetrized can be avoided. The self-trapping regime does not necessitate such a fast transformation of the potential, since its states evolve very slowly. Through this method, it was possible to create any initial population difference with a standard deviation of 0.06. In the Josephson Junction (JJ) regime, the small inter-well separation allows particles to achieve a tunneling time on the order of 40 ms (as can be seen in Fig.4.1a). This must be contrasted with the tunneling time of past realizations of BECs in double-well potentials [46, 41], which is on the order of thousands of seconds. As a consequence of the shorter time scale, Oberthaler and his group were able to be the first to make direct observations of the nonlinear dynamics in a single bosonic Josephson junction. Furthermore, it is important to note that the tunneling time of 40 ms observed in the  $^{87}\text{Rb}$  Bose-Einstein condensate in the JJ regime is much shorter than the tunneling time of 500 ms observed in the same system for noninteracting particles [1]. This observation, together with the appearance of the self-trapping phenomenon observed by the Heidelberg group, clearly indicates the importance of interatomic interactions in the tunneling process.

## 4.2 Wavepacket Dynamics: Classical Considerations

The DNLS equation, Eq. (2.12), can be used in the dynamic analysis of the underlying classical double well. In the calculations below we assume, without loss of generality, that  $\varepsilon_i = 0$ .

We start our analysis by defining the density matrix:  $\rho_{lk} = A_l A_k^*$ . Note that  $\rho_{ll} = A_l A_l^*$  is the normalized number of particles at site  $l$ ; with the normalization defined such that:  $\rho_{11} + \rho_{22} = 1$ . The population imbalance is then written as  $\rho = \rho_{11} - \rho_{22} = (n_1 - n_2)/N$ , where  $n_1$  and  $n_2$  are the number of particles at sites 1 and 2, respectively, and  $N$  is the total number of atoms. Our target in this section is to understand the time evolution of the population imbalance,  $\rho$ , and compare the outcomes of this study with the exact quantum calculations derived in §4.3.

#### 4 Dynamics of the dimer

Multiplying Eq. (2.12) by  $A_j^*$  and its complex conjugate by  $A_l$  and subtracting, we find that

$$i\dot{\rho}_{lj} = \tilde{U}\rho_{lj}(\rho_{ll} - \rho_{jj}) - k(\rho_{l+1,j} - \rho_{l,j+1} + \rho_{l-1,j} - \rho_{l,j-1}). \quad (4.1)$$

Four different possible expressions can be derived from Eq. (4.1), from the cases: (a)  $l = 1, j = 2$ , (b)  $l = 2, j = 1$ , (c)  $l = 1, j = 1$ , and (d)  $l = 2, j = 2$ :

$$\begin{aligned} \dot{\rho}_{12} &= -i\tilde{U}\rho\rho_{12} - ik\rho, & \text{for } l = 1, j = 2 & \quad (a) \\ \dot{\rho}_{21} &= i\tilde{U}\rho\rho_{21} + ik\rho, & \text{for } l = 2, j = 1 & \quad (b) \\ \dot{\rho}_{11} &= -ik(\rho_{12} - \rho_{21}), & \text{for } l = 1, j = 1 & \quad (c) \\ \dot{\rho}_{22} &= ik(\rho_{12} - \rho_{21}), & \text{for } l = 2, j = 2. & \quad (d) \end{aligned} \quad (4.2)$$

Adding Eqs. (4.2c) and (4.2d) we find that

$$\dot{\rho}_{11} + \dot{\rho}_{22} = 0 \quad (4.3)$$

indicating that  $\rho_{1,1} + \rho_{2,2}$  is a constant of motion. Therefore, since at  $t = 0$ , we know that  $\rho_{1,1} + \rho_{2,2} = 1$ , we are able to conclude that the total number of particles is conserved throughout the time evolution (see also §2.5 and Appendix A for relevant discussion). The time derivative of the population imbalance is derived by taking the difference between Eq. (4.2c) and Eq. (4.2d),

$$\dot{\rho} = \dot{\rho}_{11} - \dot{\rho}_{22} = -2ik(\rho_{12} - \rho_{21}). \quad (4.4)$$

By adding Eq. (4.2a) and (4.2b) and substituting in for  $\dot{\rho}$ , we find

$$\dot{\rho}_{12} + \dot{\rho}_{21} = \frac{\tilde{U}}{4k}\rho\dot{\rho}, \quad (4.5)$$

which simplifies to

$$\dot{\rho}_{12} + \dot{\rho}_{21} = \frac{\tilde{U}}{4k} \frac{d\rho^2}{dt}. \quad (4.6)$$

When we integrate both sides of this equation over time, we find

#### 4 Dynamics of the dimer

$$\rho_{12}(t) + \rho_{21}(t) = \frac{\tilde{U}}{4k}[\rho^2(t) - \rho^2(0)] + [\rho_{12}(0) + \rho_{21}(0)]. \quad (4.7)$$

Then we add Eq. (4.2a) and (4.2b) and again substitute in for  $\dot{\rho}$ :

$$\ddot{\rho} = -2\tilde{U}k\rho(\rho_{12} + \rho_{21}) + (2ik)^2\rho. \quad (4.8)$$

Keeping in mind that  $\rho$  is dependent on  $t$ , via Eq. (4.7) this becomes

$$\ddot{\rho}(t) = -\frac{\tilde{U}^2}{2}\rho^3(t) + \left( \frac{\tilde{U}^2}{2}\rho^2(0) - 2\tilde{U}k(\rho_{12}(0) + \rho_{21}(0)) + (2ik)^2 \right) \rho(t), \quad (4.9)$$

which is simply a differential equation,

$$\ddot{\rho}(t) = -A\rho^3(t) + B\rho(t), \quad (4.10)$$

with constants  $A = \tilde{U}^2/2$  and  $B = \frac{\tilde{U}^2}{2}\rho^2(0) - 2\tilde{U}k(\rho_{12}(0) + \rho_{21}(0)) - (2k)^2$ .

By assigning the population imbalance a meaning analogous to the position of a particle of mass  $m = 1$ , we can interpret the right-hand side of Eq. (4.10) as a nonlinear force,  $F$ , responsible for the motion of the particle. Therefore, the underlying potential is  $\mathcal{U}(\rho) = -\int F d\rho$ . Integrating over  $\rho$ , this becomes

$$\mathcal{U}(\rho) = \frac{A}{4}\rho^4(t) - \frac{B}{2}\rho^2(t). \quad (4.11)$$

Some limiting cases of the the one-dimensional motion described in Eq. (4.10) can be solved easily: (a) *The non-interacting limit* associated with  $\tilde{U} = 0$  results in Rabi-like oscillations in the population of each trap with a frequency  $\omega = 2k$ . (b) *The linear regime* for which  $\rho \ll 1$ . In this case, Eq. (4.10) describes the small amplitude oscillations of a linear pendulum. The population imbalance thus oscillates sinusoidally with the frequency  $\omega_L = \sqrt{2\tilde{U}k + 4k^2}$ .

However, in the presence of nonlinearity, the behavior is profoundly different and quite rich. Numerical solutions of Eq. (4.10) are shown in Fig. 4.2. In this figure,

#### 4 Dynamics of the dimer

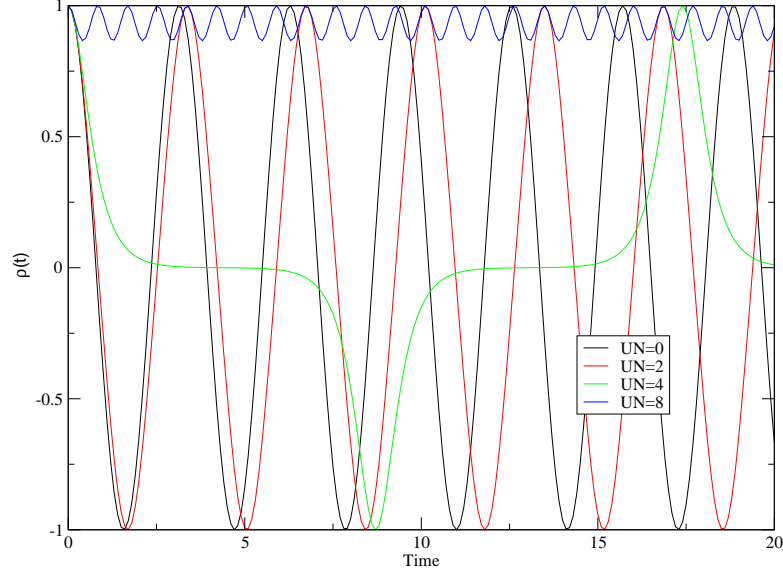


Figure 4.2: The classical behavior in the presence of a nonlinear interatomic interaction strength.

nonsinusoidal oscillations, which can be considered as the anharmonic generalization of the sinusoidal JJ effect, are evident. Moreover, an additional novel nonlinear effect occurs: a self-trapping population imbalance. Below, we present a qualitative analysis of the one-dimensional motion describe by Eq. (4.10) and explain under which conditions JJ oscillations and self-trapping occur.

We can characterize this potential by finding its zeroes. We find at which points  $\mathcal{U}(\rho) = 0$ :

$$\rho = \begin{cases} 0 \\ \pm\sqrt{\frac{2B}{A}} \quad \text{only if } B > 0. \end{cases} \quad (4.12)$$

Secondly, we determine the zeroes of  $\frac{\partial\mathcal{U}(\rho)}{\partial\rho}$ , which will reveal where the maxima and minima of  $\mathcal{U}(\rho)$  are located:

$$\rho = \begin{cases} 0 \\ \pm\sqrt{\frac{B}{A}} \quad \text{only if } B > 0. \end{cases} \quad (4.13)$$

Finally, the second derivative of the potential,  $\frac{\partial^2\mathcal{U}(\rho)}{\partial\rho^2} = 3A\rho^2(t) - B$ , allows us to

## 4 Dynamics of the dimer

ascertain for which conditions the points in Eq. (4.13) define a maximum or a minimum.

$$\begin{aligned}
 &\text{If } \rho = \pm\sqrt{\frac{B}{A}}, && \frac{\partial^2\mathcal{U}}{\partial\rho^2} \text{ is positive,} && \text{so they are minima of } \mathcal{U}(\rho). \\
 &\text{If } \rho = 0, \text{ then } \frac{\partial^2\mathcal{U}}{\partial\rho^2} = -B, \text{ thus} \\
 &\quad \text{if } B > 0 && \frac{\partial^2\mathcal{U}}{\partial\rho^2} \text{ is negative,} && \text{so it is a maximum of } \mathcal{U}(\rho). \\
 &\quad \text{if } B < 0 && \frac{\partial^2\mathcal{U}}{\partial\rho^2} \text{ is positive,} && \text{so it is a minimum of } \mathcal{U}(\rho).
 \end{aligned}$$

The Heidelberg group demonstrated the existence of three different important regimes experimentally: the JJ regime, the self-trapping regime, and the critical point. Using the characteristics of the potential shown in this section, we can calculate the ratios of interatomic interaction to coupling strength necessary to achieve these three behaviors. The quantity  $B$  characterizes these three regions. If  $B < 0$ , then we are in the JJ regime, since the potential is simply a parabola as shown in Fig. 4.3a. On the other hand, if  $B > 0$ , then as in Fig. 4.3c, we find ourselves in the self-trapping regime. Finally, the transition between the two occurs at  $B = 0$ , as in Fig. 4.3b. We assume that the initial preparation is such that all particles are in site 1 at  $t = 0$  and thus  $\rho(0) = 1$ . In this case,  $\rho_{12}(0) = \rho_{21}(0) = 0$ , and thus we find that

$$\begin{aligned}
 &|\frac{\tilde{U}}{k}| < 4 \quad \text{for the Josephson regime} \\
 &|\frac{\tilde{U}}{k}| = 4 \quad \text{for transition regime} \\
 &|\frac{\tilde{U}}{k}| > 4 \quad \text{for self-trapping regime.}
 \end{aligned} \tag{4.14}$$

### 4.3 Wave Packet Dynamics: Quantum Calculations

After having explored the classical dynamics of the dimer for different interatomic interaction strengths, we delve into the quantum time evolution of the atomic population imbalance. To this end we numerically integrate the time-dependent Schrödinger equation associated with the Hamiltonian (Eq. (3.1)) of the dimer. The evolving state is

## 4 Dynamics of the dimer

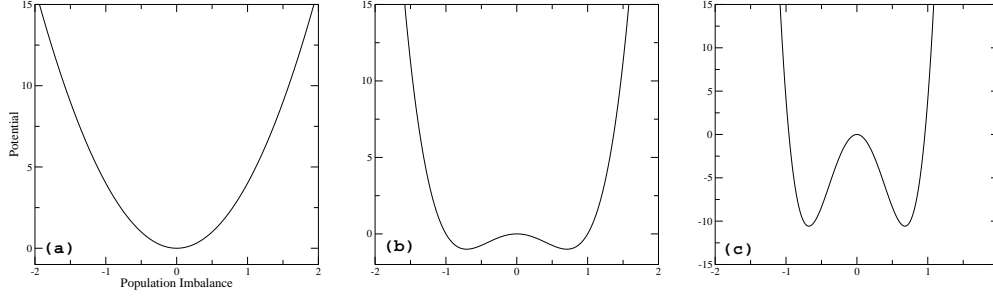


Figure 4.3: An illustration of the potential for the three dynamical regimes of the dimer.

- (a) Demonstrates the potential shape for Josephson oscillations. The ratio  $\tilde{U}/k = 0$ . (b) The transition between the JJ and self-trapping regimes, where  $\tilde{U}/k = 4$ . (c) The self-trapping regime with  $\tilde{U}/k = 10$ .

$|\psi(t)\rangle$  and we are interested in the evolving occupation distribution  $P_t(n_1) = |\psi_{n_1}(t)|^2$  where the occupation probability amplitude is defined as  $\psi_{n_1}(t) = \langle n_1 | \psi(t) \rangle$ . Here  $|n_1\rangle \equiv |n_1, N - n_1\rangle$  indicates a Fock-state (see §2.5) and  $n_1 = 0, 1, 2, \dots, N$  is the occupation on the left site. We will again discuss the case where all the bosons initially occupy one of the two wells, i.e.  $n_1(t=0) = N$  and  $n_2(t=0) = 0$ . The corresponding wave function in the Fock space is  $|\psi_0\rangle \equiv |\psi(t=0)\rangle \equiv |N, 0\rangle$ .

Now we would like to explore the various dynamical scenarios that can be generated by the Schrödinger equation for  $\psi_n(t)$ . Namely,

$$i\hbar \frac{d\psi_{n_1}(t)}{dt} = H_{n_1, n_1} \psi_{n_1}(t) + H_{n_1, n_1+1} \psi_{n_1+1}(t) + H_{n_1, n_1-1} \psi_{n_1-1}(t), \quad (4.15)$$

where  $H_{n,m}$  is given in the Fock basis by Eq. (3.2). We describe the occupation spreading profile for  $t > 0$  by the probability distribution  $P_t(n_1)$ . An impression of the evolving distribution,  $P_t(n_1)$ , will allow us to access the full counting statistics for the dimer. In particular, it is convenient to characterize the spreading profile using the various moments  $q$  of the population imbalance operator  $\langle \psi(t) | J_z^q | \psi(t) \rangle$ . The literature thus far takes a special interest in the study of the first moment  $J_z$ . An overview of the time evolution of  $\langle J_z \rangle$ , for some representative values of the interatomic interaction strength  $\tilde{U}$ , can be seen in Fig. 4.4.

#### 4 Dynamics of the dimer

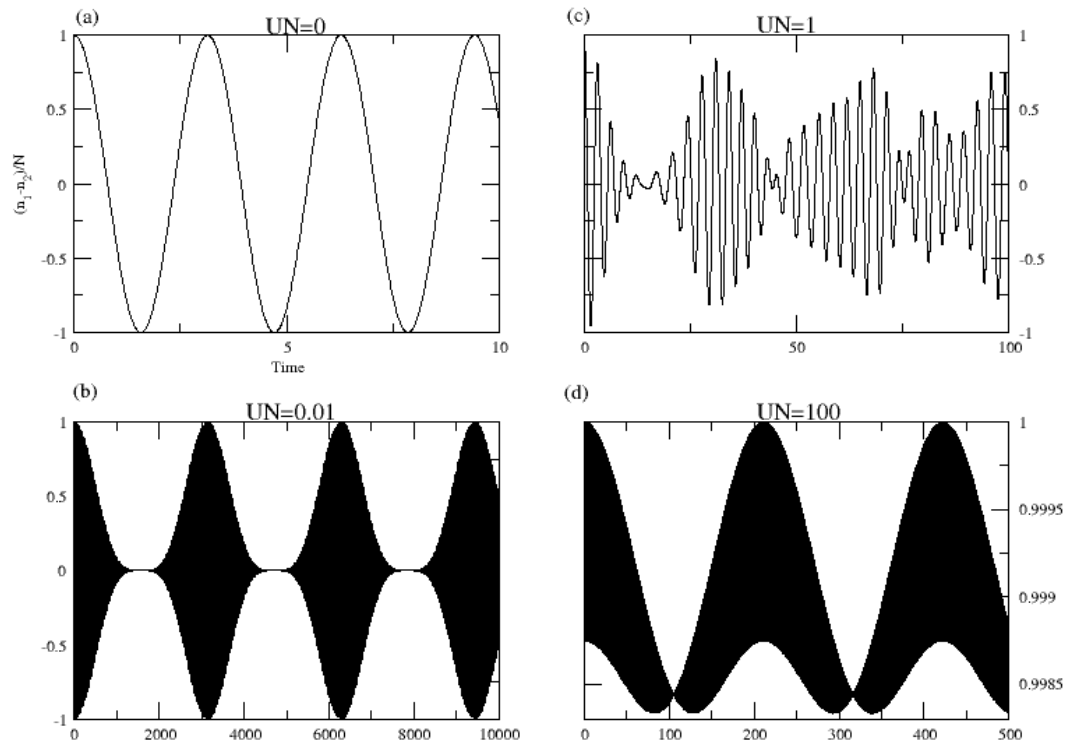


Figure 4.4: Illustrates the time evolution of the population imbalance. Note the decreasing periodicity as well as the decreasing period in figures (b) through (d).

### 4.3.1 The non-interacting limit

When we have zero interatomic interactions, simple probabilistic arguments can be used in order to produce an expression for the total occupation probability  $P_t(n_1)$  for any time  $t$ , during the evolution [43].

$$P_t^B(n_1) = \binom{N}{n_1} p^{n_1} (1-p)^{N-n_1}, \quad (4.16)$$

where  $p(t)$  is a free fitting parameter and corresponds to the normalized population at site 2. In Figures 4.6 and 4.7, we compare the numerical results of  $P_t(n_1)$  with the fitted predictions of  $P_t^B(n_1)$ . We extracted the fitting parameter,  $p(t)$ , for various  $\tilde{U}$  by fitting the distribution of the wave function with Eq. (4.16) with a maximum tolerance of 0.0001 (see Fig. 4.5). In Fig. 4.5, we observe a good agreement with the expected behavior for  $\tilde{U} = 0$ , i.e.  $\rho(t) = \frac{1}{2}(1 - \cos(2kt))$ . In fact, Figs. 4.6 and 4.7 show that the agreement with the binomial distribution (Eq. (4.16)) not only fits the non-interaction limit, but also non-zero interatomic interaction strengths for short times. In these cases,  $p(t)$  matches the results of the normalized population of site 2,  $\rho_{2,2}(t)$ , as calculated by the DNLS equation.

In order to evaluate the break time,  $t_{break}$ , above which the binomial distribution (Eq. (4.16)) no longer applies, we have introduced the following measure

$$\chi^2(t) = \sum_{n_1} |P_t(n_1) - P_t^B(n_1)|^2. \quad (4.17)$$

We have found (see Fig. 4.8) that for  $\tilde{U} \leq 1$ , the  $\chi^2(t)$  scales according to the following rule:

$$\tilde{\chi} = t^4 \text{ where } \tilde{\chi} = \chi^2 / \tilde{U}^4,$$

which suggests that the break time is

$$t_{break} \propto 1/\tilde{U} \quad (4.18)$$

## 4 Dynamics of the dimer

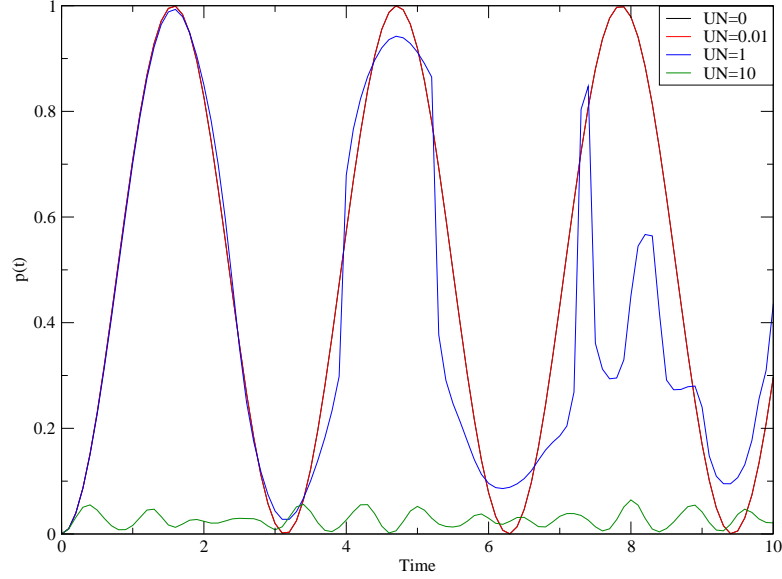


Figure 4.5: The evolution of the free fitting parameter, which corresponds to the normalized population at site 2, for different values of  $\tilde{U}$  at  $k = 1$  and  $N = 5$ . The correspondence between  $\tilde{U} = 0$  and  $\tilde{U} \neq 0$  breaks down more and more rapidly as the value of  $\tilde{U}$  increases.

For larger  $\tilde{U}$ , within the self-trapping regime  $t_{break}$  becomes larger. In the self-trapping regime, we are able to derive the distribution from perturbation theory.

### 4.3.2 The small coupling regime

We will now analyze the generated quantum dynamics for the case where the coupling between the two wells is very small, i.e. the self-trapping regime. We define the original system as one made up of two separate wells with no coupling, as in §3.3.1. We now use  $H'$  (Eq. (3.14)) to perturb the 0th order Hamiltonian for a time,  $T$ , so our full Hamiltonian is

$$H = H_0 - \delta k H' \quad (4.19)$$

At  $t = 0$ , we put all of the particles in site 1, thus  $|\psi(t = 0)\rangle \equiv |N\rangle \equiv |N, 0\rangle$ , where  $|n_1\rangle$  is in the  $H_0$  basis. Since  $\delta k$  and  $H'$  do not change over time, the time evolution operator is

## 4 Dynamics of the dimer

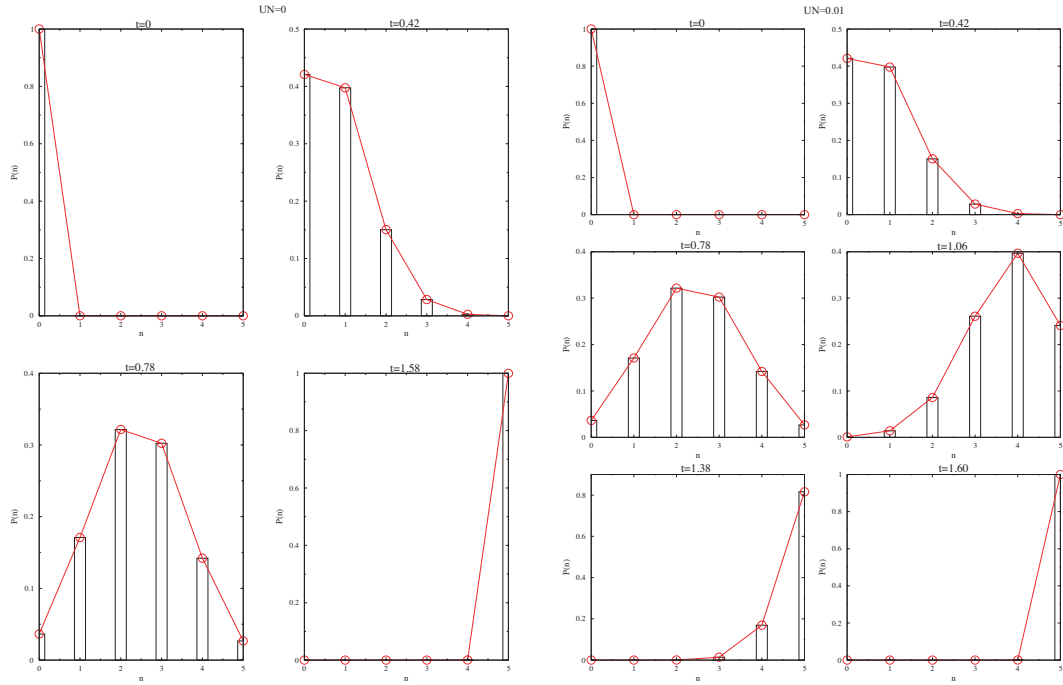


Figure 4.6: The distribution  $P_t(n_1)$  (black bars) and the fit obtained from  $P_t^B(n_1)$  (red lines). Note that in the short term, the agreement is good for all values of  $\tilde{U}$ , however, for longer times, we begin to observe deviations after the break time,  $t_{break}$ , when  $\tilde{U} \neq 0$ .

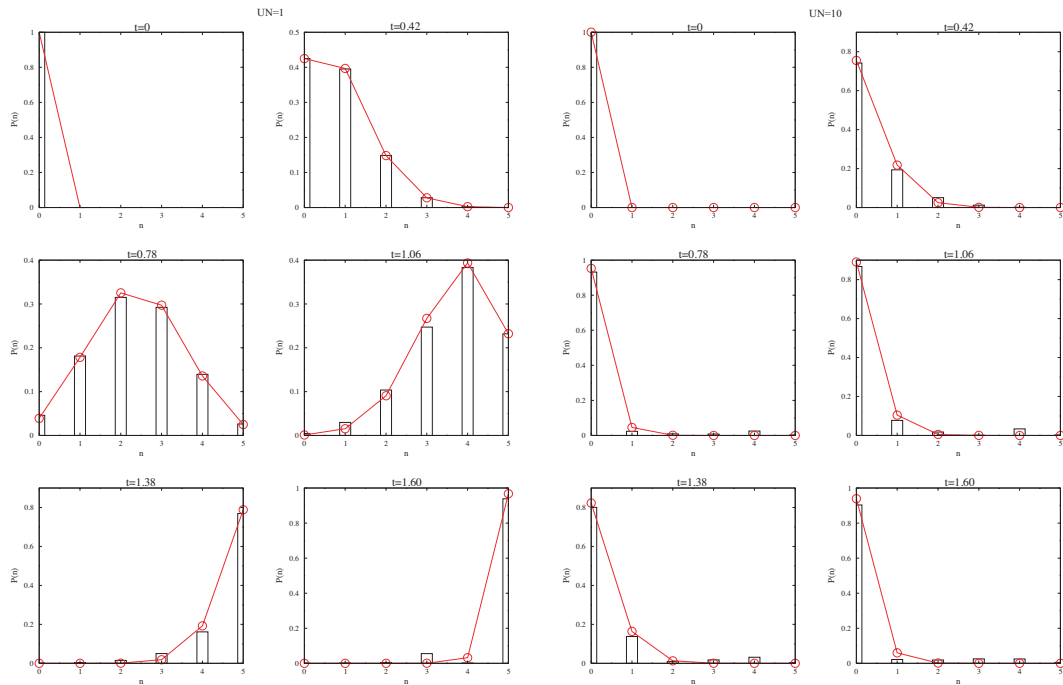


Figure 4.7: See caption from Fig. 4.6.

## 4 Dynamics of the dimer

N=5, k=1

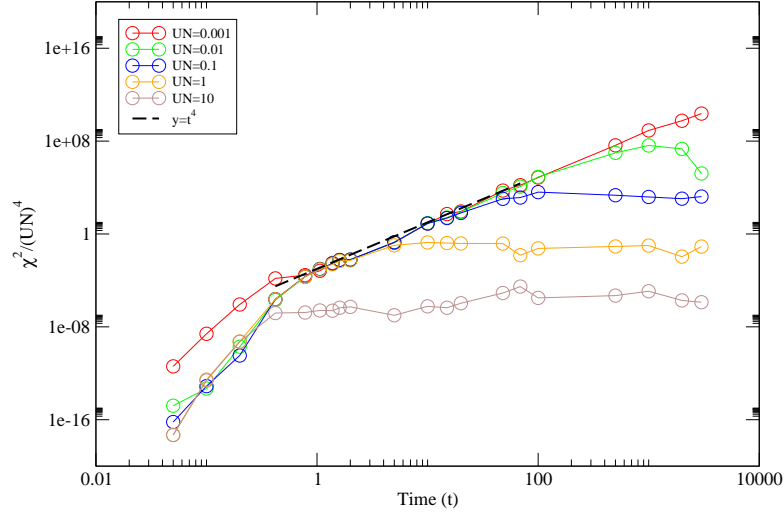


Figure 4.8: Exploring the break time by plotting  $\chi^2 = \sum_{n_1} |P_t(n_1) - P_t^B(n_1)|^2$  as obtained from fitting  $P_t^B(n_1)$  to various distributions,  $P(n_1)$ , for longer times and various values of  $\tilde{U}$ . The rescaling of the y-axis indicates a  $1/t$  behavior for the break time,  $t_{break}$ , in the regimes  $\tilde{U} \leq 1$ .

$$|\psi(t)\rangle = e^{\frac{iHt}{\hbar}} |\psi(0)\rangle, \quad (4.20)$$

where  $|\psi(t)\rangle$  is in the  $H_0$  basis. Using this structure, we are able to calculate the occupation of each site,  $\langle \psi(t) | n_i | \psi(t) \rangle$ , which allows us to calculate the population imbalance.

In Fig. 4.9, we report our numerical results for the expectation value (i.e. first moment) of the normalized population imbalance  $(n_1 - n_2)/N$ . As we discussed above, the initial preparation is such that  $n_1 = N$  and  $n_2 = 0$ . One can clearly see, that for different time scales, the dynamics exhibit quantum-specific behaviors [26]. For short times, the amplitude of the oscillations about the initial preparation is very small (see top panel of Fig. 4.9), as is to be expected from the DNLS equation (Eq. (2.12)). For small couplings we are in the self-trapping regime of the DNLS equation; however, as we move into longer times scales, such as the middle panel of Fig. 4.9, we see that, though the bosons remain localized, the quantum dynamics differs from that of the DNLS equation and exhibits collapses and complete revivals. As it was shown in Ref.

#### 4 Dynamics of the dimer

[26], the two sufficiently close frequencies which are responsible for the resulting beat at this time scale are provided by the splitting of the second highest quasi-degenerate pair of energy levels (see Chapter 3). Finally, at very large time scales (see the bottom panel of Fig. 4.9), we find that the bosons tunnel coherently between the two wells, i.e. from state  $|N, 0\rangle$  to  $|0, N\rangle$  and back, a phenomenon not encompassed by the DNLS equation at all. This behavior is due to the fact that there is no eigenstate of the system that is localized in one trap, and as a result the initial preparation has to decompose into the symmetric and antisymmetric combinations of localized states at each trap. The lifting of the degeneracy of the higher-lying energy levels provides the corresponding tunneling frequency [26].

The dynamics seen in Fig. 4.9 can be analyzed using time-dependent perturbation theory. It is simplest to approach this using the angular momentum operators as in §3.3.2. The population imbalance between the two sites is defined by the  $J_z$  operator, (Eq. (3.34)), thus we will calculate how its mean value fluctuates over time. The mean value is given by [26]:

$$\begin{aligned} \langle J_z(t) \rangle &= \langle \psi(0) | J_z | \psi(0) \rangle \\ &= \sum_{n, n'} \langle \psi(0) | h_{n'} \rangle \langle h_{n'} | e^{iHt} J_z e^{-iHt} | h_n \rangle \langle h_n | \psi(0) \rangle \end{aligned} \quad (4.21)$$

Since  $J_z |m_{\pm}\rangle = m |m_{\mp}\rangle$ , only the cross terms of differing symmetry survive, thus

$$\begin{aligned} \langle J_z(t) \rangle &= \sum_m \left[ e^{i(E_{m-} - E_{m+})t} \langle \psi(0) | h_{m-} \rangle m \langle h_{m+} | \psi(0) \rangle \right. \\ &\quad \left. + e^{i(E_{m+} - E_{m-})t} \langle \psi(0) | h_{m+} \rangle m \langle h_{m-} | \psi(0) \rangle \right] \end{aligned} \quad (4.22)$$

For 0th order, this becomes

$$\langle J_z^{(0)}(t) \rangle = \frac{N}{2}, \quad (4.23)$$

while up to second order the first moment of  $\langle J_z \rangle$  becomes

#### 4 Dynamics of the dimer

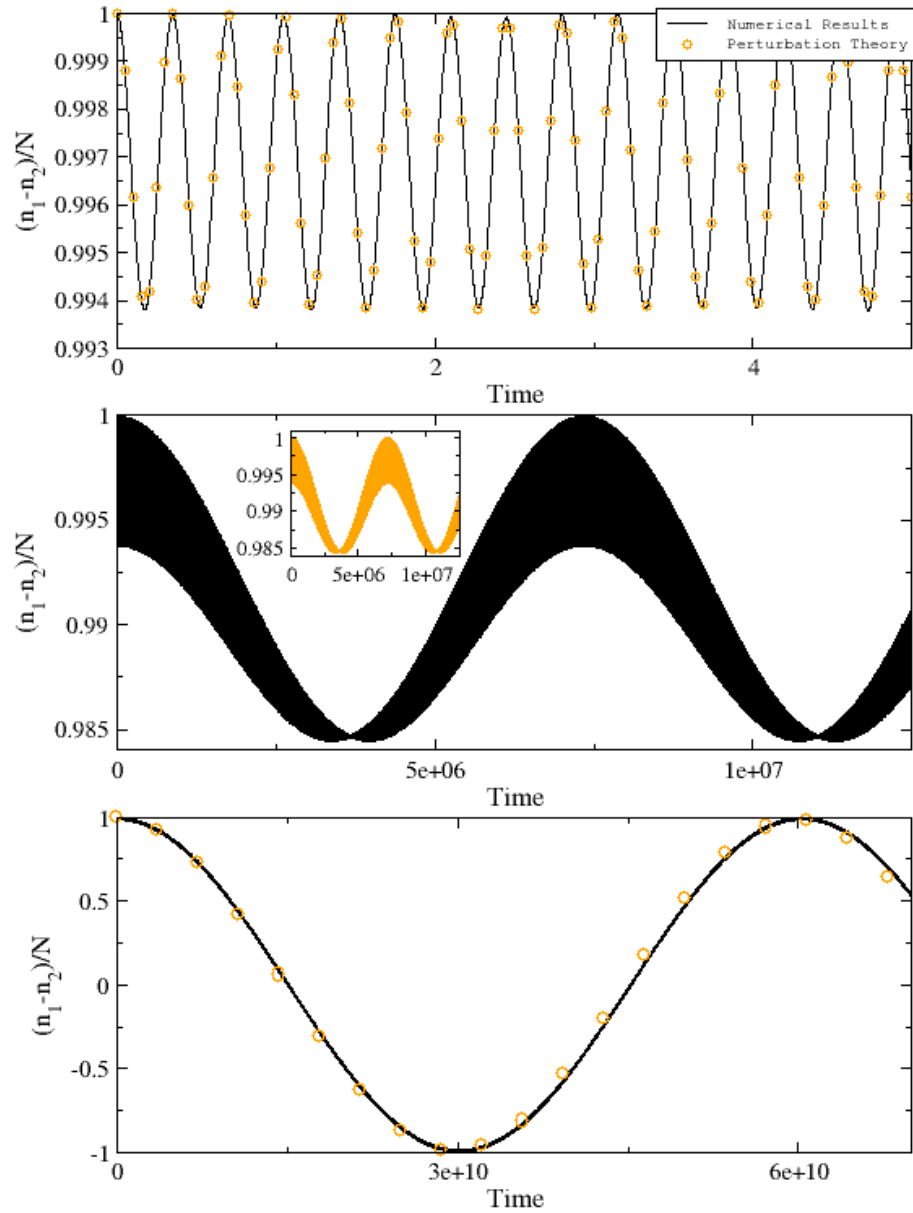


Figure 4.9: The time evolution for various time scales of a dimer system with  $N = 10$ ,  $k = 0.5$ , and  $\tilde{U} = 1$ , based on Ref. [26]. Note that though on short time scales, the localized state stays trapped, on long time scales tunneling allows the bosons to move between the wells, thus causing the states to oscillate between  $|N, 0\rangle$  and  $|0, N\rangle$ . The numerical results are in black, while the analytical results are in orange.

#### 4 Dynamics of the dimer

$$\langle J_z^{(2)}(t) \rangle = \frac{N}{2} + \frac{k^2 N}{2(N-1)^2} [\cos(\omega_\mu t) - 1], \quad (4.24)$$

where  $\omega_\mu = 2(N-1) - k^2 \frac{N+1}{N^2-4N+3}$ .

In the upper panel of Fig. 4.9, we overplot the numerical results for the normalized population imbalance  $\langle J_z \rangle / N$  and the theoretical expression (Eq. (4.24)). However, since  $\omega_\mu$  only characterizes the highest frequency,  $\langle J_z^{(2)}(t) \rangle$  cannot describe the dynamics in the longer time scales. Thus, higher orders in the perturbation theory are necessary to model the dynamics in the middle and lower panels of Fig. 4.9. Analogously to the second order calculations, we use Eq. (4.21) to calculate the higher order corrections. This results in an expression to  $N$ th order of the population imbalance [26]

$$\begin{aligned} \frac{n_1 - n_2}{N} = & - \left( \cos(\omega_0 t) + \frac{k^2}{2(N-1)^2} \left[ \frac{N}{2} [\cos(\omega_1 t) - \cos(\omega_0 t)] \right. \right. \\ & \left. \left. + 2\cos(\omega_\mu t)\cos\left(\frac{\omega_1}{2}t\right) - \cos(\omega_1 t) - \cos(\omega_0 t) \right] \right), \end{aligned} \quad (4.25)$$

where

$$\omega_0 = k^N \frac{(N-1)(N-2)}{2^{N-2}(N-1)!} \quad (4.26)$$

$$\omega_1 = k^{N-2} \frac{(N-1)(N-2)}{2^{N-4}(N-3)!}. \quad (4.27)$$

The frequencies  $\omega_0$  and  $\omega_1$  correspond to the lifting of the degeneracies  $\Delta E_{(N/2-1)\pm}$  and  $\Delta E_{(N/2)\pm}$ , respectively. The results for Eq. (4.25) are overplotted on the middle and lower panels of Fig. 4.9, where a good agreement between the numerical and perturbative results can be observed.

As we discussed at the beginning of this chapter, our goal is to understand the entire evolving probability occupation  $P_t(n)$ . To this end, we need to gain an impression of  $J_z$  (which can be easily translated to higher moments of occupation of the left well,  $n_1$ ). Unfortunately, we were not able to come out with a simple theoretical expression. Instead, a detail numerical analysis allowed us to speculate the following scaling relation [43]:

## 4 Dynamics of the dimer

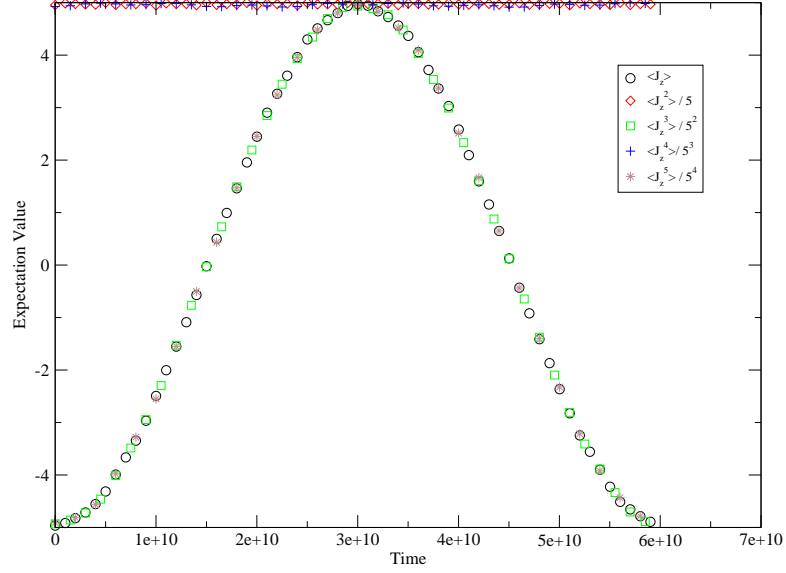


Figure 4.10: Long time behavior of the moments of  $\langle J_z \rangle$  in the self-trapped regime ( $UN=20$ ,  $k=0.5$ ,  $N=10$ ). Even and odd moments fall into two different groups and the constituents of each group scale to fit on top of one another.

$$\left\{ \begin{array}{l} \langle J_z^q \rangle = \langle J_z \rangle \left(\frac{N}{2}\right)^{q-1} \quad \text{for odd moments of } J_z \\ \langle J_z^q \rangle = \langle J_z^2 \rangle \left(\frac{N}{2}\right)^{q-1} \quad \text{for even moments of } J_z \end{array} \right. , \quad (4.28)$$

which provides the correct overall scaling for long time scales, as shown in Figs. 4.10 and 4.11. We do note, however, that although the above simple scaling relation accurately represents the scaling behavior of the various moments of  $J_z$  for long times scales, it does not provide the detailed scaling needed to capture the short time dynamics (see Fig. 4.12). Nevertheless, we have shown that, for short time scales, first order perturbation theory is applicable (for an application to the first moment, see the upper panel of Fig. 4.13).

### 4.3.3 The small interatomic interaction regime

We now turn to the analysis of the Josephson Junction regime, which is explored in Ref. [43]. As we have discussed in §4.3.1, for  $\tilde{U} = 0$ , the evolving occupation probability is

#### 4 Dynamics of the dimer

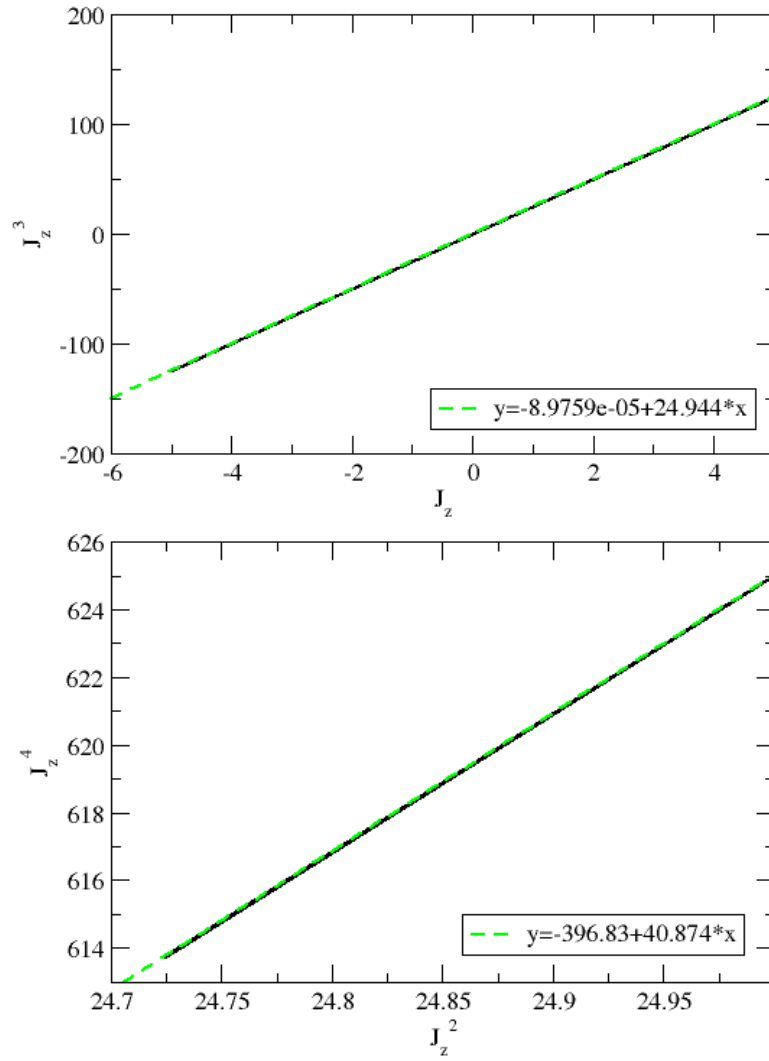


Figure 4.11: Further illustration of the long time scaling behavior of the even and odd moments of  $\langle J_z \rangle$  for the same system and time scale as in Fig. 4.10.

## 4 Dynamics of the dimer

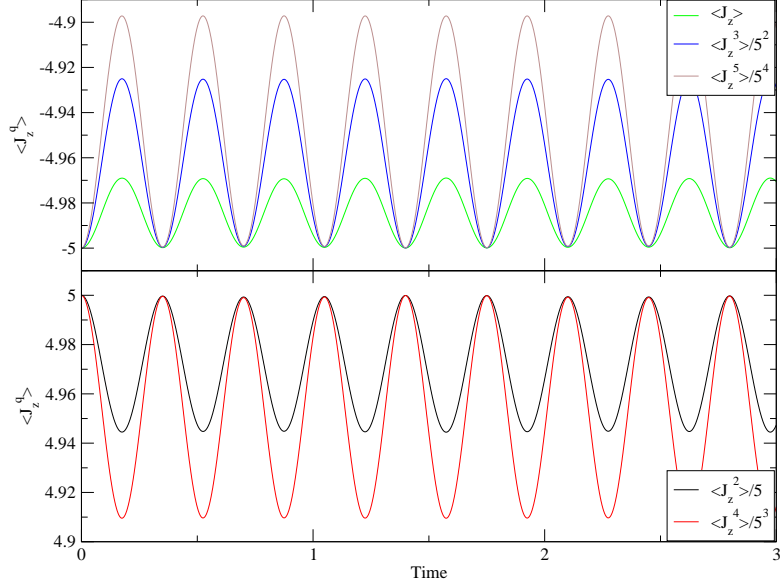


Figure 4.12: Odd and even moments of  $\langle J_z \rangle$  in the same system as Fig. 4.10. For short times, higher order perturbation theory is needed to achieve detailed scaling.

described well by the binomial distribution (Eq. (4.16)). We have also found that for  $\tilde{U} \neq 0$  describes the evolving distribution  $P_t(n_1)$  well, but for relatively short times. Thus, in this section we want to deepen our understanding of the behavior of  $P_t(n_1)$  to larger times by implementing first-order time-dependent perturbation theory. To this end, we define our 0th order Hamiltonian and perturbing Hamiltonian as in §3.3.2. To find the time evolution of the  $q$ th moment of  $J_z$ ,  $\langle J_z^q(t) \rangle$ , we again utilize Eq. (4.21), replacing the second order corrections to the wave function for the small coupling regime with the corrected wave functions in the  $J_x$ -basis for the small interaction regime (see Chapter 3):

$$\langle J_z^q(t) \rangle = \sum_{n,n'} \langle \psi(0) | n' \rangle \langle n' | e^{iHt} J_z^q e^{-iHt} | n \rangle \langle n | \psi(0) \rangle, \quad (4.29)$$

where our initial condition is the same as in §4.3.2,  $n = N/2 - n_1$  (with  $n_1$  being population at site 1), and

$$|n \rangle_x = |n^{(0)} \rangle_x + U \sum_{m \neq n} \frac{x \langle m^{(0)} | J_z^2 | n^{(0)} \rangle_x}{E_n^{(0)} - E_m^{(0)}} |m^{(0)} \rangle_x, \quad (4.30)$$

#### 4 Dynamics of the dimer

which, when we employ the  $J_z$  to  $J_x$  conversion relationship, Eq. (B.5), becomes

$$|n \rangle_z = \sum_{\alpha} A_{\alpha}^{(n)} |\alpha \rangle_z + U \sum_{m \neq n} \sum_{r,l} \frac{A_l^{(n)} A_l^{(m)} t^2}{-2k(m-n)} A_r^{(m)} |r \rangle_z. \quad (4.31)$$

By evaluating Eq. (4.29)<sup>1</sup>, we find that to first order,

$$\begin{aligned} \langle J_z^q(t) \rangle = & \sum_{n,n'} \left\{ \left[ A_{N/2}^{(n)} A_{N/2}^{(n')*} \sum_r A_r^{(n)} A_r^{(n')*} r^q + A_{N/2}^{(n)} A_{N/2}^{(n')*} U \sum_{m \neq n} \sum_{r,l} \frac{A_l^{(n)} A_l^{(m)} t^2}{-2k(m-n)} A_r^{(n')*} A_l^{(m)} r^q \right. \right. \\ & + A_{N/2}^{(n)} A_{N/2}^{(n')*} U \sum_{m' \neq n'} \sum_{r,l'} \frac{A_{l'}^{(n')*} A_{l'}^{(m')*} t^2}{-2k(m'-n')} A_r^{(m')*} A_r^{(n)} r^q \\ & + \left( \sum_r A_r^{(n)} A_r^{(n')*} r^q \right) \left( U A_{N/2}^{(n)} \sum_{m' \neq n'} \sum_{l'} \frac{A_{l'}^{(n')*} A_{l'}^{(m')*}}{-2k(m'-n')} A_{N/2}^{(m')*} \right) \\ & \left. + \left( \sum_r A_r^{(n)} A_r^{(n')*} r^q \right) \left( U A_{N/2}^{(n')*} \sum_{m \neq n} \sum_l \frac{A_l^{(n)} A_l^{(m)}}{-2k(m-n)} A_{N/2}^{(m)} \right) \right] \\ & \left. e^{i[E^{(0)}(n) + UE^{(1)}(n) - (E^{(0)}(n') + UE^{(1)}(n'))]t} \right\} \end{aligned} \quad (4.32)$$

The first moment of  $\langle J_z \rangle$  as calculated in Eq. (4.32) is contrasted with the exact quantum numerics in Fig. 4.13.

First order perturbation theory holds until the mean energy difference between neighboring energy levels of the unperturbed Hamiltonian is on the order of the strength of the perturbation. From Chapter 2, we know that the mean energy difference between is  $E_{diff} \sim n$ , where  $n = -N/2, \dots, N/2$ . Thus, the mean energy difference is on the order of  $n$ . The strength of the perturbation, according to Eq. (3.38), is on the order of  $Un^2$ . Therefore, the perturbation breaks down when  $Un^2 \geq n$ . In the case of the BHH

---

<sup>1</sup>for details, see Appendix C.1.

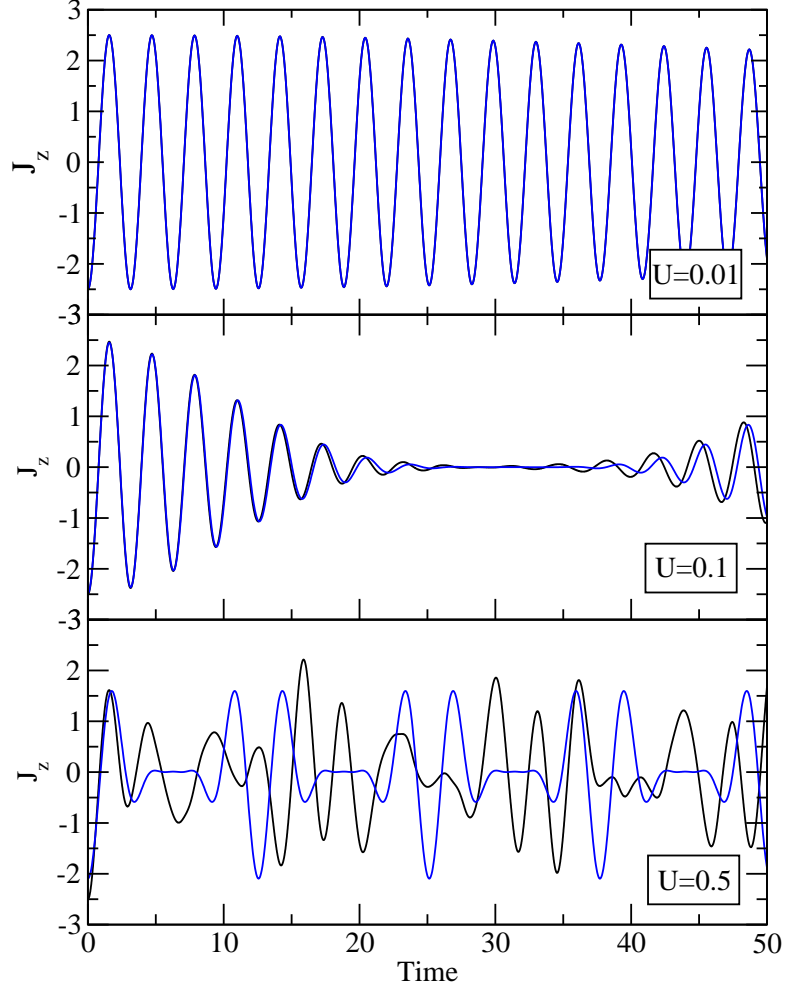


Figure 4.13: The first moment of  $\langle J_z \rangle$  for different interatomic interactions, where  $k = 1$  and  $N = 5$ . The black line was produced through quantum numerics. The blue line is the first order perturbation theory (see Eq. (4.32)).

dimer, the perturbation theory breaks first for the most excited states (i.e. when the wave function is completely localized, as in our initial preparation). Hence,  $UN \leq 1$  for the perturbation theory to be applicable. This agrees with our qualitative result from §4.3.1, in which we found that the binomial distribution gives us useful predictions of the total occupation probability when  $\tilde{U} \leq 1$ .

#### 4.4 Semiclassical Analysis

In this section we will employ a semiclassical approach, included in Ref. [43], for the analysis of the occupation probability distribution  $P_t(n_1)$ . We thus once again shift to

#### 4 Dynamics of the dimer

the SU(2) angular momentum representation (see Eqs. (3.34) and (3.35)).

The angular momentum operators commutes with the Casimir operator,  $\hat{J}^2 = (\hat{N}/2)(\hat{N}/2+1)$ . A fixed particle number thus corresponds to a fixed modulus of the angular momentum. Therefore, the corresponding classical phase space is given by the Bloch sphere  $\mathcal{S}^2$ . In this representation, the  $z$ -component of the Bloch vector describes the population imbalance between the two wells. For a quantum state with a well-defined angular momentum in the  $z$ -direction (i.e. an eigenstate of  $J_z$ ), the other two angular momentum components  $J_x$  and  $J_y$  are unknown, since they do not commute with  $J_z$ . Thus, the azimuthal angle  $\phi$ , also cannot be determined. Furthermore, a for fixed number of particles  $N$ , the dimensionality of the Hilbert space is  $N + 1$ . Thus the total phase space area is:

$$\text{span}(J_z) \times \text{span}(\phi) = (N + 1) \times 2\pi. \quad (4.33)$$

Using the more familiar notation  $S_x \equiv J_x/(N/2) = \sin(\theta) \cos(\phi)$ ,  $S_y \equiv J_y/(N/2) = \sin(\theta) \sin(\phi)$  and  $S_z \equiv J_z/(N/2) = \cos(\theta)$ , we can rewrite the above relation as

$$\text{span}(S_z) \times \text{span}(\phi) = 2 \times 2\pi \quad (4.34)$$

which is the surface area of the sphere. For large numbers of particles, the difference between  $N$  and  $N + 1$  becomes negligible. The effective  $\hbar$ ,  $\hbar_{eff}$ , is the area per state, therefore we note that  $\hbar_{eff} = 4\pi/N$ .

Next, we want to reformulate the DNLS dynamics given by Eq. (2.12), as a set of classical Hamiltonian equations. We can achieve this by parametrizing the complex amplitudes  $A_j$  as  $A_{1,2} = \sqrt{n_{1,2}} \exp(i\phi_{1,2})$ . Thus, phase difference  $\phi = \phi_1 - \phi_2$  and the fractional population difference  $S_z = \cos(\theta)$ , become

$$\dot{S}_z = -\sqrt{1 - S_z^2} \sin \phi \quad (4.35)$$

$$\dot{\phi} = \frac{\tilde{U}}{2k} S_z + \frac{S_z}{\sqrt{(1 - S_z^2)}} \cos \phi, \quad (4.36)$$

#### 4 Dynamics of the dimer

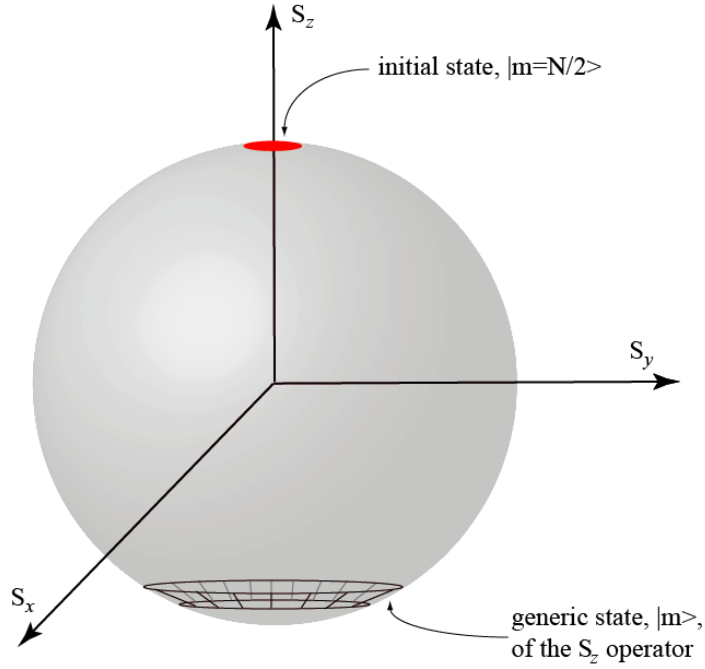


Figure 4.14: Representation of an  $|m\rangle$  state of the  $S_z$  operator in the Bloch sphere.

where the derivatives are made with respect to  $\tilde{t} = 2kt$ . The  $S_z$ ,  $\phi$  variables are canonically conjugate, with  $\dot{S}_z = -\partial H/\partial\phi$  and  $\dot{\phi} = \partial H/\partial S_z$ , where the Hamiltonian is given by [42]

$$H = \frac{\tilde{U}}{4k} S_z^2 - \sqrt{1 - S_z^2} \cos(\phi). \quad (4.37)$$

Using the  $\theta - \phi$  uncertainty relation we can conclude that any  $S_z$  (or  $J_z$  state) is represented on the Bloch sphere by an annulus of width  $\delta\theta = 2/(N+1)$  and circumference  $2\pi$ . The case of an initial state  $S_z = 1$  (where all particles are on the "left" well), is represented by a cap of area  $4\pi/(N+1)$  centered at the "north pole." An illustration of the state vectors on the Bloch sphere can be seen in Fig. 4.14.

A classical phase space distribution  $P_t^{\text{cl}}(s_z, \phi) dS_z d\phi$  describes the probability that an ensemble of particles will be found in an infinitely small phase space element,  $dS_z d\phi$ . The dynamics of the Hamiltonian,  $H$ , are governed by the classical Liouville equation

$$\frac{dP_t^{\text{cl}}(s_z, \phi)}{dt} = \frac{\partial P_t^{\text{cl}}(s_z, \phi)}{\partial t} + \{P_t^{\text{cl}}(s_z, \phi), H_{\text{PB}}\} = 0 \quad (4.38)$$

where  $\{\dots\}$  denote the classical Poisson brackets. One can evaluate the Liouvillian flow directly by making use of a classical phase space ensemble as shown in Fig. 4.15. At  $t = 0$ , the ensemble is generated by  $10^4$  phase space points to mimic the quantum distribution. Afterwards all the trajectories evolve according to the classical equation, Eq. (4.37), or the DNLS equation.

Using the outcome of the semiclassical approach we have evaluated the population imbalance in Fig. 4.16. In the same figure, we compare our results with the actual quantum calculations and the outcomes of the classical (one trajectory) analysis. Clearly, we see that the semiclassical approach captures various features of the quantum evolution. In fact, the agreement seems to persist for relatively large times and interatomic interaction strengths,  $\tilde{U}$ , as opposed to both the "one-trajectory" classical calculations and with the results of binomial distribution/first order perturbation theory, which break down after a relatively short time.

Inspired by the excellent agreement shown between the semiclassical calculations and the exact quantum results in the first moment (described by the population imbalance), shown Fig. 4.16, we would like to investigate the applicability of semiclassical methods to describe the full occupation distribution,  $P_t(n_1)$ . In Fig. 4.17, we compare the semiclassical distribution,  $P_t^{\text{cl}}(n_1)$ , with the exact quantum mechanical results,  $P_t(n_1)$ , between which we observe a reasonably good agreement.

We have shown that we can describe the dynamics of a quantum state using classical evolution schemes, where, however, one has to consider an *ensemble* of phase space trajectories propagating according to the classical equations of motion. Standard mean-field schemes, on the other hand, consider the evolution of only one trajectory. In the latter case, past literature has shown that there is a breakdown of the mean-field approximation, as shown in Fig. 4.16. (See Ref. [48].)

## 4 Dynamics of the dimer

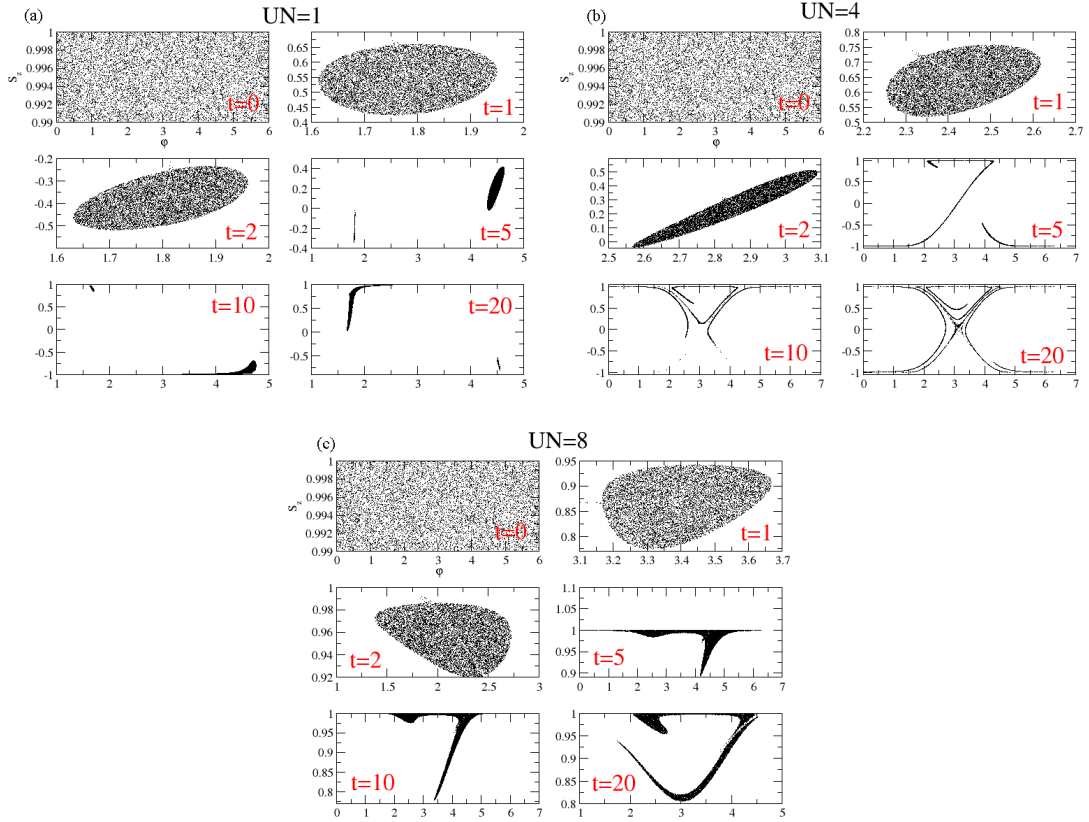


Figure 4.15: Snapshots of the evolving phase space distribution of an initial preparation associated with the quantum state  $|N, 0\rangle$ . The semiclassical distribution consist of  $10^4$  trajectories which are prepared as discussed in the text. (a)  $\tilde{U} = 1$ , corresponding to the JJ regime. (b) Transition point  $\tilde{U} = 4$ . (c) Self-trapping regime,  $\tilde{U} = 8$ .

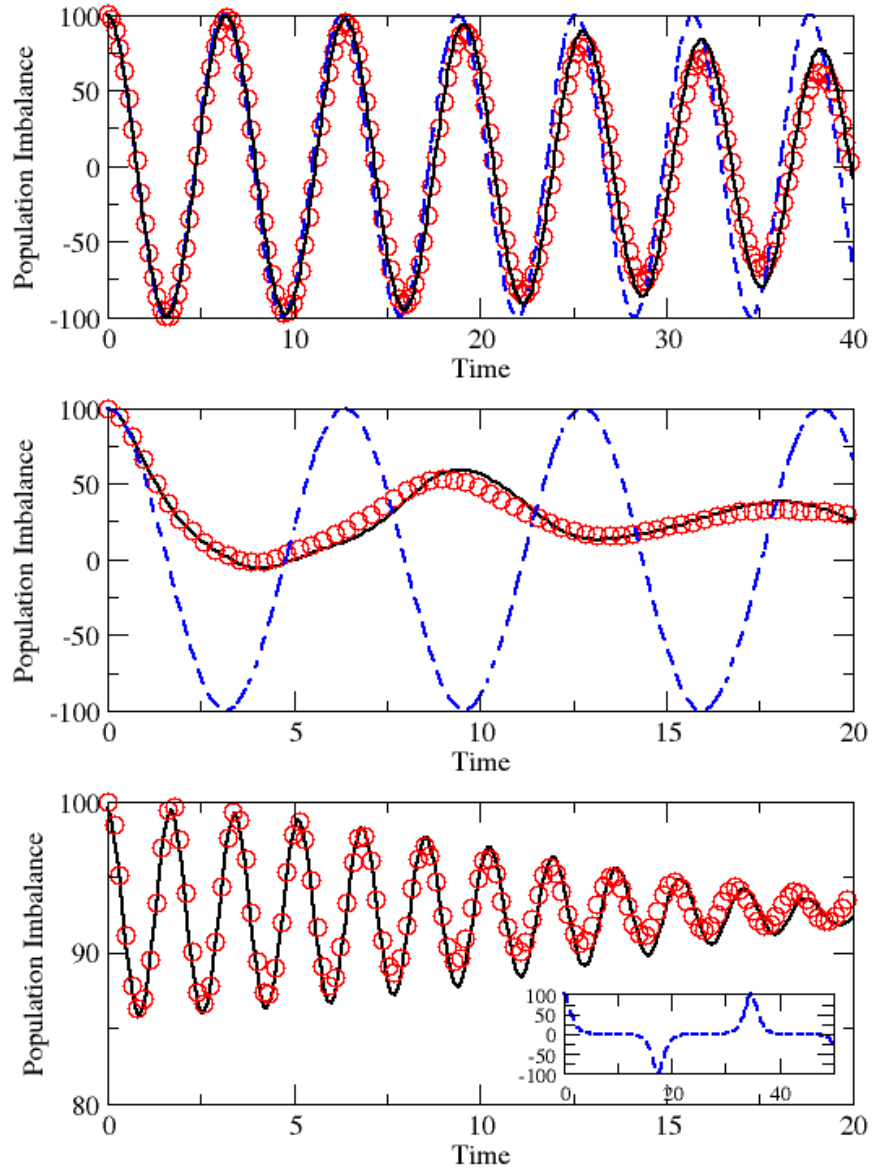


Figure 4.16: The temporal evolution of atomic population imbalance,  $n_1 - n_2$ , for various values of  $\tilde{U} = UN$ , where  $N = 100$ . The quantum numerical results are shown as red circles, while the semiclassical calculations are black lines. The initial ensemble consists of  $10^4$  trajectories and populates the "north pole cap" (as discussed in the text). The classical results (only one trajectory), as shown in Fig. 4.2, are illustrated as blue dotted lines here to emphasize the discrepancies between the DNLS solutions and the semiclassical results.

## 4 Dynamics of the dimer

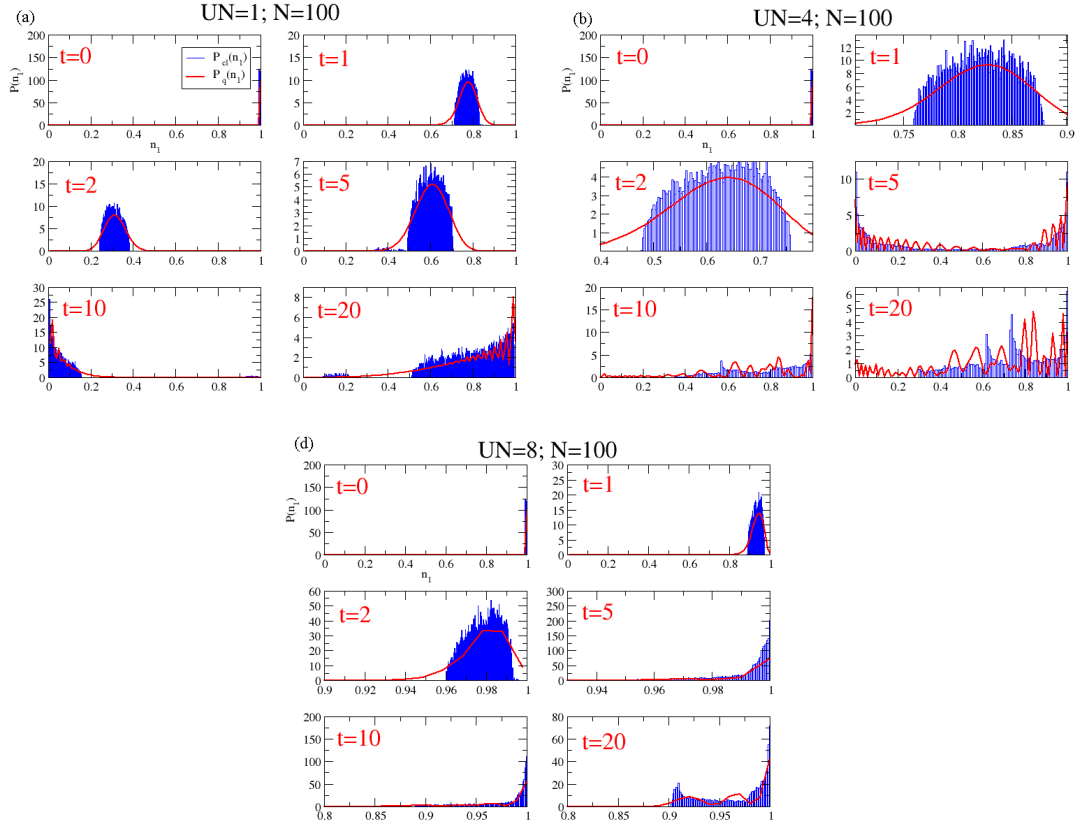


Figure 4.17: The semiclassical and the quantum evolving occupation probability. The classical results are shown as blue histograms while the quantum results are shown as red lines. A good quantum-classical correspondence is evident even for relatively large times. (a) Josephson oscillations,  $\tilde{U} = 1$ . (b) Transition point,  $\tilde{U} = 4$ . (c) Self-trapping regime,  $\tilde{U} = 8$ .

## 5 Conclusions

We have investigated the effects of interatomic interactions on the full occupation probability of an evolving Bose-Einstein condensate of ultra-cold atoms loaded in a deep double well potential. Such a study provides information on the fluctuations of the occupation number and on the probabilistic nature of the quantum mechanical transmission/reflection process experienced by the atoms when they move between wells.

Specifically, we use perturbation theory both for small interatomic interaction strengths and small coupling strengths, to explore the dynamics of the dimer. In addition, we delve into the higher moments of the quantum fluctuations of the atomic populations, thereby finding a scaling behavior between them. The limits of the validity of the perturbation theory are given and checked numerically. In addition, we suggest a semiclassical phase space analysis based on the evolution of an ensemble of trajectories, which nicely captures all of the essential features of the quantum dynamics.

The analysis of the wavepacket dynamics of the quantum dimer is the first step towards understanding more complicated dynamical scenarios. One case of future interest for us is the problem of counting statistics in multipath geometries, the simplest example of which is the quantum trimer. We expect that the results of this and future work will be easily confirmed experimentally due to the rapid development of highly accurate measurement techniques recently developed for ultra-cold BECs.

# A Quantum Mechanical Conservation of the Total Number of Particles, $N$ , in the Dimer

The Hamiltonian used to describe the BEC dimer is the BHH to second quantization (Eq. (2.3)).

$$\hat{H} = \sum_{i=1}^s \varepsilon_i \hat{n}_i + \frac{1}{2} \sum_{i=1}^s U_i \hat{n}_i (\hat{n}_i - 1) - \sum_{i,j}^s k_{i,j} [\hat{b}_i^\dagger \hat{b}_j + \hat{b}_j^\dagger \hat{b}_i], \quad (\text{A.1})$$

where  $[n_i, n_j] = 0$ ,  $[n_i, b_j] = [n_i, b_j^\dagger] = 0$ , and  $[b_i, b_j^\dagger] = \delta_{ij}$ . The commutation relation between the Hamiltonian,  $\hat{H}$ , and the operator counting the number of particles in the system,  $\hat{N}$ , is

$$[\hat{H}, \hat{N}] = \hat{H}\hat{N} - \hat{N}\hat{H}. \quad (\text{A.2})$$

The expectation value of the commutation relation is

$$\begin{aligned} \langle m | [\hat{H}, \hat{N}] | m \rangle &= \langle m | \hat{H}\hat{N} | m \rangle - \langle m | \hat{N}\hat{H} | m \rangle \\ &= N(\langle m | \hat{H} | m \rangle - \langle m | \hat{H} | m \rangle) \\ &= 0 \end{aligned} \quad (\text{A.3})$$

In order to find how this relates to  $\partial N / \partial t$ , we need to use the standard definition for a time average, which is

$$\langle A(t) \rangle = \langle \psi(t) | A(t) | \psi(t) \rangle, \quad (\text{A.4})$$

thus

$$\begin{aligned} \frac{\partial}{\partial t} \langle A(t) \rangle &= \left[ \frac{\partial}{\partial t} \langle \psi(t) | \right] A(t) | \psi(t) \rangle + \langle \psi(t) | \left[ \frac{\partial}{\partial t} A(t) \right] | \psi(t) \rangle + \langle \psi(t) | A(t) | \left[ \frac{\partial}{\partial t} | \psi(t) \rangle \right] \\ &= \frac{i}{\hbar} \langle \psi(t) | H A(t) | \psi(t) \rangle - \frac{i}{\hbar} \langle \psi(t) | A(t) H | \psi(t) \rangle + \langle \psi(t) | \left[ \frac{\partial}{\partial t} A(t) \right] | \psi(t) \rangle \\ &= \frac{i}{\hbar} \langle \psi(t) | [H, A] | \psi(t) \rangle + \langle \psi(t) | \left[ \frac{\partial}{\partial t} A(t) \right] | \psi(t) \rangle \\ &= \frac{i}{\hbar} \langle [H, A] \rangle + \frac{\partial}{\partial t} \langle A \rangle. \end{aligned} \quad (\text{A.5})$$

Thus, since  $\partial \langle N \rangle / \partial t = 0$ ,

$$\frac{\partial}{\partial t} \langle N(t) \rangle = \frac{i}{\hbar} \langle [\hat{H}, \hat{N}] \rangle = 0, \quad (\text{A.6})$$

as in §2.5.

## B Perturbation Theory in the Small Nonlinear Interaction Regime

We begin by writing our unperturbed and perturbing Hamiltonians in the angular momentum representation. The angular momentum operators are defined as [25]:

$$J_x = \frac{1}{2}(b_1^\dagger b_2 + b_2^\dagger b_1), \quad J_y = \frac{i}{2}(b_1^\dagger b_2 - b_2^\dagger b_1), \quad J_z = \frac{1}{2}(b_2^\dagger b_2 - b_1^\dagger b_1) \quad (\text{B.1})$$

and

$$J^2 = \frac{N}{2} \left( \frac{N}{2} + 1 \right). \quad (\text{B.2})$$

Thus, the unperturbed Hamiltonian, in this case, is that part of the BHH associated with the coupling strength,

$$H_0 = -2kJ_x, \quad (\text{B.3})$$

while the perturbing Hamiltonian is

$$H' = \frac{U}{2} J_z^2. \quad (\text{B.4})$$

In order to do the perturbation, we needed to move to the  $J_x$ -basis. We thus convert the vectors used to span the Fock-state as described in §2.5 into the  $J_z$ -basis. An arbitrary vector in the  $J_x$ -basis can be written as a superposition of the eigenstates of the  $J_z$ -basis via the relationship [34]

$$|j, m \rangle_x = \sum_{n=-j}^j A_n^{(m)} |j, n \rangle_z, \quad (\text{B.5})$$

*B Perturbation Theory in the Small Nonlinear Interaction Regime*

where

$$A_n^{(m)} = 2^n \left[ \frac{(j+n)!(j-n)!}{(j+m)!(j-m)!} \right]^{1/2} P_{j+n}^{(m-n, -m-n)}(0), \quad (\text{B.6})$$

in which  $P_n^{(\alpha, \beta)}(z)$  is the Rodriguez formula for Jacobi polynomials

$$P_n^{(\alpha, \beta)}(z) = [(-1)^n / 2^n n!] [(1-z)^\alpha (1+z)^\beta]^{-1} \frac{d^n}{dz^n} [(1-z)^{\alpha+n} (1+z)^{\beta+n}]. \quad (\text{B.7})$$

As before, since in the dimer,  $j$  and  $m$  are linked by  $N = j + m$ , we say  $|m \rangle \equiv |j, m \rangle$ .

Note that  $J_x |n \rangle_x = n |n \rangle_x$ .

In perturbation theory, the exact energies can be approximated by a sum of the various energy corrections:

$$E_n = E_n^{(0)} + \frac{U}{2} E_n^{(1)} + \left( \frac{U}{2} \right)^2 E_n^{(2)} + \dots \quad (\text{B.8})$$

The 0th order energy is

$$E_n^{(0)} = {}_x \langle n | H_0 | n \rangle_x = -2kn \quad (\text{B.9})$$

The first order energy corrections are given by standard perturbation theory to be

$$E_n^{(1)} = {}_x \langle n | H' | n \rangle_x, \quad (\text{B.10})$$

which, via B.5 becomes

$$\begin{aligned} E_n^{(1)} &= \sum_{m, m'} A_m^{(n)*} A_{m'}^{(n)} {}_z \langle m | J_z^2 | m' \rangle_z \\ &= \sum_{m, m'} A_m^{(n)*} A_{m'}^{(n)} m'^2 {}_z \langle m | m' \rangle_z \\ &= \sum_m |A_m^{(n)}|^2 m^2 \end{aligned} \quad (\text{B.11})$$

The first order wavefunction corrections are given by

$$\psi_n^{(1)} = \sum_{m \neq n} \frac{\langle \psi_m^{(0)} | H' | \psi_n^{(0)} \rangle}{E_n^{(0)} - E_m^{(0)}} \psi_m^{(0)} \quad (\text{B.12})$$

which becomes

$$\begin{aligned}
 \psi_n^{(1)} &= \sum_{m \neq n} \frac{x \langle m | H' | m \rangle_x}{-2k(m-n)} |m\rangle_x \\
 &= \sum_{m \neq n, l, l'} \sum \frac{A_{l'}^{(n)} A_l^{(m)*} \langle z | J_z^2 | l' \rangle_z}{-2k(m-n)} \sum_r A_r^{(m)} |r\rangle_z \\
 &= \sum_{m \neq n, l, l'} \sum \frac{A_{l'}^{(n)} A_l^{(m)*} l^2 \langle z | l | l' \rangle_z}{-2k(m-n)} \sum_r A_r^{(m)} |r\rangle_z \\
 &= \sum_{m \neq n, l, r} \sum \frac{A_{l'}^{(n)} A_l^{(m)*} l^2}{-2k(m-n)} A_r^{(m)} |r\rangle_z .
 \end{aligned} \tag{B.13}$$

# C The Time Evolution of $J_z$ to First Order in Small Interatomic Interaction Perturbation Theory

As in the section on time-independent perturbation theory in the small interatomic interaction region, we use the angular momentum representation of the unperturbed and perturbing Hamiltonians (see Appendix B). The mean value is given by [26]:

$$\langle J_z^q(t) \rangle = \sum_{n,n'} \langle \psi(0) | n \rangle \langle n | e^{iHt} J_z^q e^{-iHt} | n' \rangle \langle n' | \psi(0) \rangle_z, \quad (\text{C.1})$$

where  $|\psi(0)\rangle \equiv |N, 0\rangle$  and

$$\begin{aligned} |n\rangle &= |n^{(0)}\rangle_x + U \sum_{m \neq n} \frac{\langle m^{(0)} | J_z^2 | n^{(0)} \rangle_x}{E_n^{(0)} - E_m^{(0)}} |m^{(0)}\rangle_x \\ &= \sum_{\alpha} A_{\alpha}^{(n)} |\alpha\rangle_z + U \sum_{m \neq n} \sum_{r,l} \frac{A_l^{(n)} A_l^{(m)} l^2}{-2k(m-n)} A_r^{(m)} |r\rangle_z \end{aligned} \quad (\text{C.2})$$

via the  $J_z$ -basis to  $J_x$ -basis conversion defined in Eq. (B.5), where the indices of  $A_n^{(m)}$  are equal to  $N/2 - n_1$ .

First we calculate the terms  $\langle \psi(0) | n \rangle$  and  $\langle n | \psi(0) \rangle_z$ :

$$\begin{aligned}
{}_z \langle \psi(0) | n \rangle &= ({}_z \langle n | \psi(0) \rangle_z)^* = {}_z \langle N, 0 | \left[ \sum_{\alpha} A_{\alpha}^{(n)} | \alpha \rangle_z + U \sum_{m \neq n} \sum_{r,l} \frac{A_l^{(n)} A_l^{(m)} l^2}{-2k(m-n)} A_r^{(m)} | r \rangle_z \right] \\
&= \sum_{\alpha} A_{\alpha}^{(n)} {}_z \langle N, 0 | \alpha \rangle_z + U \sum_{m \neq n} \sum_{r,l} \frac{A_l^{(n)} A_l^{(m)} l^2}{-2k(m-n)} A_r^{(m)} {}_z \langle N, 0 | r \rangle_z \\
&= A_{N/2}^{(n)} + U \sum_{m \neq n} \sum_l \frac{A_l^{(n)} A_l^{(m)} l^2}{-2k(m-n)} A_{N/2}^{(m)}.
\end{aligned} \tag{C.3}$$

We then calculate the effect of  $J_z^q$  on  $|n'\rangle$

$$J_z^q |n'\rangle = \sum_{\alpha} A_{\alpha}^{(n')} \alpha^q | \alpha \rangle_z + U \sum_{m' \neq n'} \sum_{r',l'} \frac{A_{l'}^{(n')} A_{l'}^{(m')} l'^2}{-2k(m'-n')} A_{r'}^{(m')} | r' \rangle_z \tag{C.4}$$

Thus,

$$\begin{aligned}
{}_z \langle n | J_z^q | n' \rangle &= \sum_r A_r^{(n)} A_r^{(n')*} r^q + U \sum_{m \neq n} \sum_{r,l} \frac{A_l^{(n)} A_l^{(m)} l^2}{-2k(m-n)} A_r^{(m)} A_r^{(n')*} r^q \\
&+ U \sum_{m' \neq n'} \sum_{r',l'} \frac{A_{l'}^{(n')*} A_{l'}^{(m')*} l'^2}{-2k(m'-n')} A_{r'}^{(m')*} A_r^{(n)} r^q.
\end{aligned} \tag{C.5}$$

The time dependent factor becomes

$$e^{i(E_n^{(1)} - E_{n'}^{(1)})t} = e^{i[E^{(0)}(n) + UE^{(1)}(n) - (E^{(0)}(n') + UE^{(1)}(n'))]t}. \tag{C.6}$$

Combining all of these elements as dictated by Eq. (C.1), we find that to first order,

$$\begin{aligned}
\langle J_z^q(t) \rangle = & \sum_{n,n'} \left\{ \left[ A_{N/2}^{(n)} A_{N/2}^{(n')*} \sum_r A_r^{(n)} A_r^{(n')*} r^q + A_{N/2}^{(n)} A_{N/2}^{(n')*} U \sum_{m \neq n} \sum_{r,l} \frac{A_l^{(n)} A_l^{(m)} l^2}{-2k(m-n)} A_r^{(n')*} A_l^{(m)} r^q \right. \right. \\
& + A_{N/2}^{(n)} A_{N/2}^{(n')*} U \sum_{m' \neq n'} \sum_{r,l'} \frac{A_{l'}^{(n')*} A_{l'}^{(m')*} l'^2}{-2k(m'-n')} A_r^{(m')*} A_r^{(n)} r^q \\
& + \left( \sum_r A_r^{(n)} A_r^{(n')*} r^q \right) \left( U A_{N/2}^{(n)} \sum_{m' \neq n'} \sum_{l'} \frac{A_{l'}^{(n')*} A_{l'}^{(m')*}}{-2k(m'-n')} A_{N/2}^{(m')*} \right) \\
& \left. + \left( \sum_r A_r^{(n)} A_r^{(n')*} r^q \right) \left( U A_{N/2}^{(n')*} \sum_{m \neq n} \sum_l \frac{A_l^{(n)} A_l^{(m)}}{-2k(m-n)} A_{N/2}^{(m)} \right) \right] \\
& e^{i[E^{(0)}(n) + U E^{(1)}(n) - (E^{(0)}(n') + U E^{(1)}(n'))]t} \Big\}, \tag{C.7}
\end{aligned}$$

where all of the  $U^2$  and higher terms have been ignored.

# Bibliography

- [1] Albiez, M., Gati, R., Folling, J., Hunsmann, S., Cristiani, M., and Oberthaler, M. K. Direct Observation of Tunneling and Nonlinear Self-Trapping in a Single Bosonic Josephson Junction. *Physical Review Letters* **95**, 010402 (2005).
- [2] Anderson, B. P. and Kasevich, M. A. Macroscopic Quantum Interference from Atomic Tunnel Arrays. *Science* **282**, 1686 (1998).
- [3] Anderson, M. H., Ensher, J. R., Matthews, M. R., Wieman, C. E., and Cornell, E. A. Observation of Bose-Einstein Condensation in a Dilute Atomic Vapor. *Science* **269**, 198 (1995).
- [4] Bernstein, L., Eilbeck, J. C., and Scott, A. C. The quantum theory of local modes in a coupled system of nonlinear oscillators. *Nonlinearity* **3**, 293 (1990).
- [5] Bose, S. N. Plancks Gesetz und Lichtquantenhypothese. *Z. Phys. A* **26**, 178 (1924).
- [6] Cataliotti, F. S., Burger, S., Fort, C., Maddaloni, P., Minardi, F., Trombettoni, A., Smerzi, A., and Inguscio, M. Josephson Junction Arrays with Bose-Einstein Condensates. *Science* **293**, 843 (2001).
- [7] Cataliotti, F. S., Burger, S., Fort, C., Maddaloni, P., Minardi, F., Trombettoni, A., Smerzi, A., and Inguscio, M. Josephson Junction Arrays with Bose-Einstein Condensates. *Science* **293**, 842 (2001).
- [8] Chefles, A. Nearest-neighbour level spacings for the non-periodic discrete nonlinear schrödinger equation. *Journal of Physics A: Mathematical and General* **29**, 4515 (1996).

## Bibliography

- [9] Cohen-Tannoudji, C. N. Nobel lecture: Manipulating atoms with photons. *Rev. Mod. Phys.* **70**, 707 (1998).
- [10] Cohen-Tannoudji, C. N. and Phillips, W. D. New mechanisms for laser cooling. *Physics Today* **43**, p33 (1990).
- [11] Cruzeiro-Hansson, L., Feddersen, H., Flesch, R., Christiansen, P. L., Salerno, M., and Scott, A. C. Classical and quantum analysis of chaos in the discrete self-trapping equation. *Phys. Rev. B* **42**, 522 (1990).
- [12] Dalfovo, F., Giorgini, S., Pitaevskii, L. P., and Stringari, S. Theory of bose-einstein condensation in trapped gases. *Rev. Mod. Phys.* **71**, 463 (1999).
- [13] Davis, K. B., Mewes, M. O., Andrews, M. R., van Druten, N. J., Durfee, D. S., Kurn, D. M., and Ketterle, W. Bose-Einstein Condensation in a Gas of Sodium Atoms. *Phys. Rev. Lett.* **75**, 3969 (1995).
- [14] Eilbeck, J. C., Lomdahl, P. S., and Scott, A. C. The Discrete Self-Trapping Equation. *Physica D* **16**, 318 (1985).
- [15] Einstein, A. Quantentheorie des einatomigen idealen Gases. *Sitzungsberg. Preuss. Akad. Wiss., Phys. Math. K.* page 261 (1924).
- [16] Einstein, A. Quantentheorie des einatomigen idealen Gases - Zweite Ausgabe. *Sitzungsberg. Preuss. Akad. Wiss., Phys. Math. K.* page 3 (1925).
- [17] Fazio, R. and van der Zant, H. Quantum phase transitions and vortex dynamics in superconducting networks. *Physics Reports* **355**, 235 (2001).
- [18] Feddersen, H. Localization of vibrational energy in globular protein. *Physics Letters A* **154**, 391 (1991).
- [19] Fritz, J., Baller, M. K., Lang, H. P., Rothuizen, H., Vettiger, P., Meyer, E., Guntherodt, H.-J., Gerber, Ch., and Gimzewski, J. K. Translating biomolecular recognition into nanomechanics. *Science* **288**, 316 (2000).
- [20] Haake, F. *Quantum Signatures of Chaos*. Springer (1991).

## Bibliography

- [21] Hagle, E. W., Deng, L., Kozuma, M., Wen, J., Helmerson, K., Rolston, S. L., and Phillips, W. D. A Well-Collimated Quasi-Continuous Atom Laser. *Science* **283**, 1706 (1999).
- [22] Hansel, W., Hommelhoff, P., Hansch, T. W., and Reichel, J. Bose-einstein condensation on a microelectronic chip. *Nature* **413**, 498 (2001).
- [23] Hennig, D. and Tsironis, G. P. Wave transmission in nonlinear lattices. *Physics Reports* **307**, 333 (1999).
- [24] Hiller, M. Parametric Bose-Hubbard Hamiltonians: Quantum Dissipation, Irreversibility, and Pumping (2007).
- [25] Kalosakas, G. and Bishop, A. R. Small-tunneling-amplitude Boson-Hubbard dimer: Stationary states. *Phys. Rev. A* **65** (2002).
- [26] Kalosakas, G., Bishop, A. R., and Kenkre, V. M. Multiple-timescale quantum dynamics of many interacting bosons in a dimer. *J. Phys. B* **36**, 3233 (2003).
- [27] Kalosakas, G., Bishop, A. R., and Kenkre, V. M. Small-tunneling-amplitude boson-hubbard dimer. ii. dynamics. *Phys. Rev. A* **68**, 023602 (2003).
- [28] Ketterle, W. Nobel lecture: When atoms behave as waves: Bose-Einstein Condensation and the atom laser. *Rev. Mod. Phys.* **74**, 1131 (2002).
- [29] Kragh, H. Max Planck, the reluctant revolutionary. *Physics World* **13**.
- [30] Leggett, A. J. Bose-Einstein Condensation in the Alkali Gases: Some fundamental concepts. *Rev. Mod. Phys.* **73**, 307 (2001).
- [31] Likharev, K. K. Superconducting weak links. *Rev. Mod. Phys.* **51**, 101 (1979).
- [32] Micheli, A., Daley, A. J., Jaksch, D., and Zoller, P. Single atom transistor in a 1d optical lattice. *Physical Review Letters* **93**, 140408 (2004).
- [33] Morsch, O. and Oberthaler, M. Dynamics of Bose-Einstein Condensates in Optical Lattices. *Rev. Mod. Phys.* **78**, 179 (pages 37) (2006).

## Bibliography

- [34] Narducci, L. M. and Orszag, M. Eigenvalues and eigenvectors of angular momentum operator  $j_x$  without the theory of rotations. *American Journal of Physics* **40**, 1811 (1972).
- [35] Orzel, C., Tuchman, A. K., Fenselau, M. L., Yasuda, M., and Kasevich, M. A. Squeezed States in a Bose-Einstein Condensate. *Science* **291**, 010402 (2001).
- [36] Pereverzev, S. V., Loshak, A., Backhaus, S., Davis, J. C., and Packard, R. E. Quantum oscillations between two weakly coupled reservoirs of superfluid  $^3\text{He}$ . *Nature* **388**, 449 (1997).
- [37] Salerno, M. and Scott, A. C. Quantum theories for two discrete nonlinear schrodinger equations. *Nonlinearity* **4**, 853 (1991).
- [38] Schmiedmayer, J., Folman, R., and Calarco, T. Quantum information processing with neutral atoms on an atom chip. *Journal of Modern Optics* **49**, 1375 (2002).
- [39] Schumm, T., Hofferberth, S., Andersson, L. M., Wildermuth, S., Groth, S., Bar-Joseph, I., Schmiedmayer, J., and Kruger, P. Matter-wave interferometry in a double well on an atom chip. *Nat Phys* **1**, 57 (2005).
- [40] Scott, A. C., Lomdahl, P. S., and Eilbeck, J. C. Between the local-mode and normal-mode limits. *Chemical Physics Letters* **113**, 29 (1985).
- [41] Shin, Y., Saba, M., Schirotzek, A., Pasquini, T. A., Leanhardt, A. E., Pritchard, D. E., and Ketterle, W. Distillation of Bose-Einstein Condensates in a Double-Well Potential. *Physical Review Letters* **92**, 150401 (2004).
- [42] Smerzi, A., Fantoni, S., Giovanazzi, S., and Shenoy, S. R. Quantum coherent atomic tunneling between two trapped bose-einstein condensates. *Phys. Rev. Lett.* **79**, 4950 (1997).
- [43] Smith-Mannschott, K., Chuchem, M., Hiller, M., Cohen, D., and Kottos, T. Counting statistics for the Wavepacket Dynamics of a single bosonic Josephson Junction. *in preparation* (2008).

## Bibliography

- [44] Stenger, J., Stamper-Kurn, D. M., Andrews, M. R., Chikkatur, A. P., Inouye, S., Miesner, H.-J., and Ketterle, W. Optically Confined Bose-Einstein Condensates. *J. Low Temp. Phys.* **113**, 167 (1998).
- [45] Sukhatme, K., Mukharsky, Y., Chui, T., and Pearson, D. Observation of the ideal josephson effect in superfluid 4He. *Nature* **411**, 280 (2001).
- [46] Tiecke, T. G., Kemmann, M., Buggle, C., Shvarchuck, I., von Klitzing, W., and Walraven, J. T. M. Bose-Einstein condensation in a magnetic double-well potential. *Journal of Optics B: Quantum and Semiclassical Optics* **5**, S119 (2003).
- [47] Townsend, C., Ketterle, W., and Stringari, S. Bose-Einstein condensation. *Physics World* (1997).
- [48] Vardi, A. and Anglin, J. R. Bose-einstein condensates beyond mean field theory: Quantum backreaction as decoherence. *Phys. Rev. Lett.* **86**, 568 (2001).
- [49] Wright, E., Eilbeck, J. C., Hays, M. H., Miller, P. D., and Scott, A. C. The quantum discrete self-trapping equation in the Hartree approximation. *Physica D* **69**, 18 (1993).